Plasma-driven Non-oxidative Coupling of Methane to Ethylene and Hydrogen at Mild Temperature over Cu_xO/CeO_2 Catalyst

Rui Liu,[1,] Shangkun Li,[1, 2,] Qian Chen,[1] Dongxing Li,[1] Jiasong Zhao,[1] Chuang Li,[1] Xiaoxia Gao,[3] Wenping Zhao,[4] Li Wang,[5] Chong Peng,[1] Annemie Bogaerts,[2] Hongchen Guo,[1, *] Yanhui Yi [1, *]

[1]State Key Laboratory of Fine Chemicals, Frontier Science Center for Smart Materials, School of Chemical Engineering, Dalian University of Technology, Dalian, 116024, P.R. China.
[2]Research group PLASMANT, Department of Chemistry, University of Antwerp, Universiteitsplein 1, BE-2610 Wilrijk-Antwerp, Belgium.
[3]Instrumental Analysis Center, Dalian University of Technology, Dalian, 116024, P.R. China.
[4]China Tianchen Engineering Corporation, Tianjin, 300409, P.R. China.
[5]College of Environmental Sciences and Engineering, Dalian Maritime University, Dalian 116026, Liaoning, China

*Corresponding Author: hongchenguo@163.com; yiyanhui@dlut.edu.cn

Abstract:

We report one-step non-oxidative coupling of methane (CH_4) to ethylene (C_2H_4) at atmospheric pressure and mild temperature (ca. 180-190 °C), by a combination of non-thermal plasma and a CuO_x/CeO_2 catalyst. The C_2H_4 selectivity gradually increases during an induction period. The corresponding spent catalysts at different stages were systematically characterized to disclose the evolution of the CuO_x/CeO_2 catalyst. During the induction period, the CuO/CeO_2 catalyst was partially reduced to generate Cu^+, Ce^{3+} and O_v species, which accompany the formation of Cu^+-O_v-Ce^{3+} sites, as proven by XRD, HRTEM, XPS, Raman, EPR and H_2-TPR. In addition, the C_2H_4 selectivity is proportional to the fraction of Cu^+, Ce^{3+}, O_v and Cu-O-Ce species, which indicates that Cu^+-O_v-Ce^{3+} is the active site for non-oxidative coupling of CH_4 to C_2H_4. Furthermore, *in-situ* FTIR results indicate that the Cu^+-O_v-Ce^{3+} interface sites can promote dehydrogenation of CH_3^* (from CH_4 plasma) to produce CH_2^* on the catalyst surface, which is the basic reason why CuO_x/CeO_2 acts as a catalyst in speeding up the non-oxidative coupling of CH_4 for C_2H_4 production.

Keywords: Methane; Non-oxidative Coupling; Plasma Catalysis; Ethylene; Copper-Ceria catalyst

Introduction

The direct conversion of methane (CH_4) to ethylene (C_2H_4) is an important chemical process.[1-3] Generally, CH_4 to C_2H_4 conversion can be achieved by two approaches, i.e., oxidative coupling of methane (OCM) and non-oxidative coupling of methane (NOCM). In OCM, reactive oxygen species, typically originating from O_2, are utilized to effectively activate CH_4, which is not limited by thermodynamics (Reaction 1).[4-6] However, the OCM route cannot prevent the formation of CO_2, upon full oxidation of CH_4, which limits the yield of C_2H_4.[7-9] In contrast, the NOCM route avoids overoxidation, leading to less CO_2 emission and high carbon utilization efficiency, but it is limited by thermodynamics (Reaction 2). Hence, it has to be operated at very high temperature (> 1000 °C).[10-12]

$$CH_4\,(g) + 1/2O_2(g) \rightarrow 1/2\; C_2H_4\,(g) + H_2O\,(g) \qquad \Delta G^{\ominus}(298.15K) = -154\ kJ/mol \qquad (1)$$

$$CH_4\;\;(g) \rightarrow 1/2\; C_2H_4\;\;(g) + H_2\,(g) \qquad \Delta G^{\ominus}(298.15K) = 35\ kJ/mol \qquad (2)$$

Plasma provides a unique approach to enable some thermodynamically unfavorable chemical reactions.[13-17] In the NOCM process driven by plasma, CH_4 can be activated through inelastic collisions with energetic electrons to form radicals, which enable CH_4 conversion to produce hydrocarbons.[18] The NOCM process has been explored both by (quasi-)thermal and non-thermal plasma.[19-21] In thermal and quasi-thermal plasma, the products are dominated by acetylene (C_2H_2) and coke,[22-24] while in non-thermal plasma, the main products are ethane (C_2H_6) and propane (C_3H_8).[25-27]

Two-step processes have been investigated by a combination of plasma (hybrid plasma catalysis) and post-plasma catalysis for CH_4 conversion to C_2H_4. For instance, Delikonstantis et al., reported that CH_4 was firstly converted into C_2H_2 by a nanosecond pulsed discharge, reaching up to 23.5% yield (single pass). Subsequently, C_2H_2 was hydrogenated to C_2H_4 over a Pd/Al_2O_3 catalyst located in the post-plasma region. Overall, C_2H_4 is formed as major product at 25.7% yield.[28] Wang et al. reported a similar work, but use stable kilohertz spark discharges and a $Pd\text{-}Ag/SiO_2$ catalyst, achieving 17.1% C_2H_4 concentration and 62.6% hydrogen concentration with a specific input energy of 38.4 kJ/L.[29] Liu et al. exploited a two-stage plasma system (plasma stage + thermal cracking stage) for direct NOCM to C_2H_4, achieving 10.8% C_2H_4 yield. [30] After adding Pt/ZrO_2 catalyst in the plasma stage, C_2H_4 yield has been improved to 18.5%, while the temperature in the thermal cracking stage had to be higher than 800 °C.[31] In addition, one-step hybrid non-thermal plasma systems have also been investigated. Liu et al. performed NOCM in a dielectric barrier discharge (DBD) plasma reactor packed by Pt/CeO_2 single atom catalyst, obtaining 39% CH_4 conversion and 54% C_2 selectivity with 54 W input power. However, C_2H_4 selectivity was only 5.4 %.[32] Sungkwon Jo et al. investigated CH_4 activation in a planar-type DBD reactor, which achieved 16 % CH_4 conversion with selectivity towards C_2H_6 and C_2H_4 being 45 % and 8 %, respectively.[33] Noteworthy, Ma et al. demonstrated the direct conversion of CH_4 to C_2H_4 using a non-thermal (DBD) plasma packed by a metal-organic framework material, i.e., MFM-300(Fe).[34] At 10 % conversion, they achieved a selectivity of over 98 % for C_2 hydrocarbons, with 58% for C_2H_4. This impressive outcome was realized with a specific energy input (SEI) of 2 kJ/L and a feed gas containing only 1% CH_4 in helium. Remarkably, the authors obtained a notably high C_2H_4 selectivity of 47% solely through plasma activation without any catalysts. Therefore, the catalytic role of MFM-300(Fe) is not obvious.

We can conclude that the one-step plasma-catalytic selective conversion of CH_4 to C_2H_4 has not yet been exploited under more practical reaction conditions with wide CH_4 content and mild reaction temperature. In DBD plasma-based CH_4 conversion, the $CH_3\cdot$ generated from CH_4 plasma tend to form C_2H_6 rather than undergoing dehydrogenation to $CH_2\cdot$. That is, the direct CH_4-to-C_2H_4 conversion is still a critical challenge, since dehydrogenation of $CH_3\cdot$ into $CH_2\cdot$ is not straightforward. Therefore, seeking a catalyst to promote $CH_3\cdot$ dehydrogenation into $CH_2\cdot$, leading to C_2H_4 formation, is a very desirable route and an interesting topic. However, a suitable catalyst has not yet been found.

More insight in the optimal catalyst can be obtained by computational (microkinetic) modeling of the catalytic surface reactions, as demonstrated by Engelmann et al. for NOCM.[35] The model predicted that when vibrational excitation of CH_4 is dominant, C_2H_4 formation is promoted on most transition metal catalysts (e.g., Pt, Rh, Pd and Cu), while C_2H_6 was the dominant product on the more noble catalysts (like Ag). However, in DBD plasmas, the $CH_x\cdot$ are more abundant than vibrationally excited molecules, and they give rise to predominantly C_2H_4 formation at all transition metal catalysts investigated. Therefore, the authors concluded that the optimal catalyst material depends on (i) the desired products and (ii) the plasma conditions.[35] However, the study was limited to transition metals,[35] and the situation might be different for metal oxide catalysts, for which no model could be developed yet, due to the lack of sufficient input data.

In the present paper, we study the performance of a metal oxide catalyst. Specially, we report an efficient CuO_x/CeO_2 catalyst, on which the Cu^+-O_v-Ce^{3+} site at the Cu-CeO_2 interface is capable of promoting CH_3^* dehydrogenation to form CH_2^* species, which promote C-C coupling for one-step plasma-catalytic CH_4-to-C_2H_4 conversion. In the reaction process, we found a distinct induction period (2 hours), during which the gradually formed Cu^+-O_v-Ce^{3+} active site leads to enhancement of C_2H_4 selectivity from 5 % to 36 %. Furthermore, we have characterized the corresponding spent catalysts at different stages, to disclose the evolution of the CuO_x/CeO_2 catalyst, and in combination with *in-situ* FTIR spectra, we are able to reveal the reaction mechanism. The experimental setup of NOCM driven by non-thermal plasma catalysis is explained in the Supporting Information (SI; section 1), and shown in Figure S1 and Figure S2 (for the *in-situ* FTIR). The experimental details of the catalyst preparation and characterization are also provided in the SI (section 2).

Results and Discussion

Figure 1A illustrates the stable performance of NOCM in the case of “plasma alone”. 14.4 % CH_4 conversion is achieved, with C_2H_6 (44.5 % selectivity) being the dominant product and 44.2 % H_2 selectivity, while the selectivity to C_2H_4 is less than 5 %. In the case of “plasma + CeO_2” (plasma packed by CeO_2 granules, which belongs to non-porous material, as shown in Table S1 and Figure S3), also stable NOCM reaction performance is achieved, with 6.5 % CH_4 conversion, 30.3 % C_2H_6 selectivity and 10.6 % C_2H_4 selectivity, and 58.1 % H_2 selectivity, as shown in Figure 1B. Interestingly, in the case of “plasma + CuO/CeO_2”, as shown in Figure 1C, there is a distinct induction period of ca. 2 h, during which the C_2H_4 selectivity increases from 3.4 % to 36.1 %, while the C_2H_6 selectivity decreases from 41.6 % to 26.3 %, meanwhile, the H_2 selectivity increased from 41.6 % to 54.3 %, before reaching a steady state. The yields of C2 hydrocarbons and H_2 are also shown in Figure 1. Even at similar CH_4 conversion, the results in Figure S4 confirm that the CuO/CeO_2 catalyst is effective for producing C_2H_4 (Figure S4). The NOCM performances of initial state and steady state in the case of "plasma + CuO/CeO_2" are shown in Figure S5. Notably, the coke selectivity increases from 12.4% in the initial state to 23.1% in the steady state, and this may be caused by increased C_2H_4 selectivity since C_2H_4 is much easier to form coke than C_2H_6. The total product distribution and reaction stability for NOCM under Plasma+CuO/CeO_2 system can be found in Figure S6 and Figure S7. The GC results for C_2H_6 and C_2H_4 were presented in Figure S8. In the steady state, the C_2H_4 selectivity in case of "Plasma + CuO/CeO_2" (after 115 mins) is around 7 times the selectivity of "Plasma alone" and 3.6 times the selectivity of "Plasma + CeO_2". However, the CH_4 conversion drops from 14.4 % (Plasma alone) to 6.5 % (Plasma + CeO_2) and 6.2 % (Plasma + CuO/CeO_2), respectively. Notably, although the CH_4 conversion between "Plasma + CeO_2" and "Plasma + CuO/CeO_2" is similar, the C_2H_4 selectivity is dramatically improved, which demonstrates that CuO/CeO_2 is an efficient catalyst for plasma-catalytic one-step CH_4 conversion to C_2H_4. The predominant reaction pathways for the conversion of CH_4 to C_2 hydrocarbons by DBD plasma are shown in Figure S9, and the main electron impact reactions are listed in Table S2. The reaction conditions for the entire paper and SI (unless mentioned otherwise) are: 10 wt. % Cu loading, CH_4/Ar = 1:1, flow rate = 20 ml/min.

Correspondingly, the *in-situ* mass spectrometry signals of the products are shown in the bottom panels. For the cases of "plasma alone" and "plasma + CeO_2", the signals of m/z = 28 (C_2H_4, C_2H_6 and C_3H_8), 30 (C_2H_6), 44 (C_3H_8) and 2 (H_2) are relatively stable, which further demonstrates the stable reaction performance with low C_2H_4 selectivity. For the case of "plasma + CuO/CeO_2", the signals of m/z = 30 (C_2H_6) and 44 (C_3H_8) gradually decrease, while the signals of m/z = 28 (C_2H_4, C_2H_6 and C_3H_8) and 2 (H_2) rapidly increase after plasma is switched on. These results further indicate the improvement of C_2H_4 selectivity in the induction period.

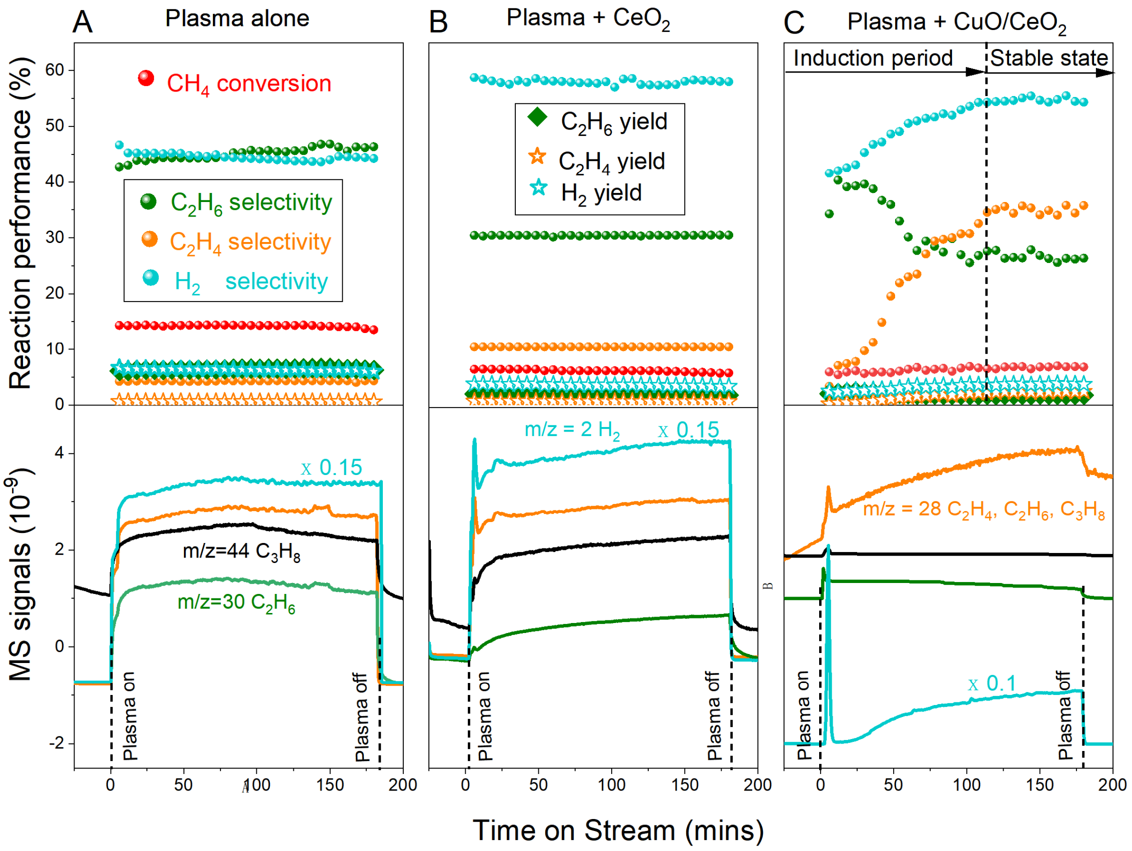

Figure 1. Reaction performance of NOCM. (A) Plasma alone, (B) Plasma + CeO_2, and (C) Plasma + CuO/CeO_2 (Reaction conditions: 10 wt. % Cu loading, CH_4/Ar = 1:1, flow rate = 20 ml/min, 1.08 g catalyst, and WHSV=1.39 h^{-1}, 15-16 W input power, 14 kHz discharge frequency.)

To better understand the above results, we first studied the plasma behavior using an oscilloscope and optical emission spectra (OES). The recorded discharge parameters in the cases of "Plasma alone", "Plasma + CeO_2" and "Plasma + CuO/CeO_2" are shown in Figure S10. It can be seen that the three cases exhibit similar discharge power (15.4-16.1 W), calculated from the Lissajous plots, although they have different discharge voltages and discharge currents. Figure S11 shows the OES of the CH_4/Ar plasma in the case of "Plasma alone", "Plasma + CeO_2" and "Plasma + CuO/CeO_2". Generally, the OES intensity of "Plasma alone" is higher than for "Plasma + CeO_2" and "Plasma + CuO/CeO_2", which is caused by the shielding effect of the granules packed in the plasma. In the OES, we observe lines assigned to CH· (314, 390 and 431.1 nm) and H· (434.1 and 486.1 nm) species, as well as many bands attributed to excited Ar and N_2 . The bands of excited N_2 molecules arise from air surface discharge between the grounded electrode and the outside wall of the reactor. Importantly, the appearance of CH· lines demonstrates the existence of CH_x· in the plasma. Furthermore, CH· are usually generated by stepwise dehydrogenation of CH_4, i.e., $CH_4 \rightarrow CH_3\cdot \rightarrow CH_2\cdot \rightarrow CH\cdot$, and the probability of generating CH_3·, CH_2· and CH· was estimated to be 79 %, 15 % and 5 %, respectively.[36] Therefore, the existence of CH· means that also CH_3· are abundant in the plasma. That is, CH_4 is activated by the plasma to produce abundant CH_3· and H atoms.

Secondly, we applied several catalyst characterization techniques, including X-ray powder diffraction (XRD), high-resolution transmission electron microscopy (HRTEM), X-ray photoelectron spectroscopy (XPS), Raman spectroscopy, electron paramagnetic resonance (EPR) and hydrogen temperature programmed reduction (H_2-TPR) to disclose the evolution of the CuO_x/CeO_2 catalyst during the induction period. Figure 2A shows the XRD patterns of the fresh and spent CuO/CeO_2 catalysts. In addition to typical peaks of fluorite CeO_2, two weak peaks at 35.5 and 38.7 degrees, attributed to the (002) and (111) plane of CuO, respectively, are collected for the fresh and spent CuO/CeO_2 catalysts at different stages. However, the local magnification results (Figure 2B) indicate that the peaks of Cu_2O (111) and Cu (111) do not appear for the fresh sample, but arise for the spent samples, and the diffraction intensity gradually increases during the two-hour induction period. This result demonstrates a partial reduction of CuO to Cu_2O and Cu during the induction period. Moreover, the diffraction pattern reflections of CeO_2 systematically shifted to higher degree in CuO/CeO_2-Fresh catalyst in Figure S12, suggesting that Cu^{2+} has been substituted into the CeO_2 lattice [37] and altered the unit cell parameter of CeO_2,[38,39] because of the smaller ionic radius of Cu^{2+} (0.073 nm) than that of Ce^{4+} (0.097nm), and a Cu-Ce solid solution might be formed.[40-44] The drop of lattice parameter calculated by XRD is presented in Table S3. However, the lattice parameters of CeO_2 in CuO/CeO_2-0.5h, CuO/CeO_2-1h, and CuO/CeO_2-2h catalysts in this experiment are larger, which could be explained because the modified metal and copper enter the CeO_2 lattice, accompanied by the formation of more Ce^{3+}, and the ionic radius of Ce^{3+} (0.110 nm) was larger than the ionic radius of Ce^{4+}, which led to the larger cell parameters.[45]

Figure 2C illustrates the HRTEM image of fresh CuO/CeO_2 catalyst, while Figures 2 D, E and F present the HRTEM images of spent CuO/CeO_2 catalysts after 0.5, 1 and 2 h reaction, respectively. For the fresh CuO/CeO_2 catalyst, only CuO (111) lattice fringes can be observed. In the images of the spent sample after 0.5 and 1 h reaction, however, both Cu_2O (111) and CuO (002) species appear. Notably, for the spent CuO/CeO_2 catalyst after 2 h reaction, fully reduced metallic Cu species (i.e., Cu (111) surface) is observed. These HRTEM images further verify the gradual reduction of CuO into Cu_2O and metallic Cu species during the induction period, which is consistent with the XRD results. Moreover, the boundary area formed between copper oxide species and ceria in CuO/CeO_2-2h catalyst is shown in Figure 2 (G-I). In Figure 2H, the inter-planar spacing of the distinct lattice fringe is measured to be about 0.31 nm, which matches well with the (111) crystal planes of the cubic CeO_2 structure. The spacing of lattice fringes around 0.255 is ascribed to the (002) crystallographic planes of CuO. It means that some CuO_x particles exist independently around the CeO_2 particles,[37] which form the CuO_x-ceria interface. The red square in Fig. 2I also illustrates the interfaces between Cu and CeO_2 displaying the distortion of the CeO_2 lattice, which suggests that Cu species have been incorporated into the CeO_2 lattice to form the Cu-O-Ce structure. Both the copper substitution and the CuO_x-ceria boundary could lead to the formation of the Cu-[O]-Ce species.[46-48]

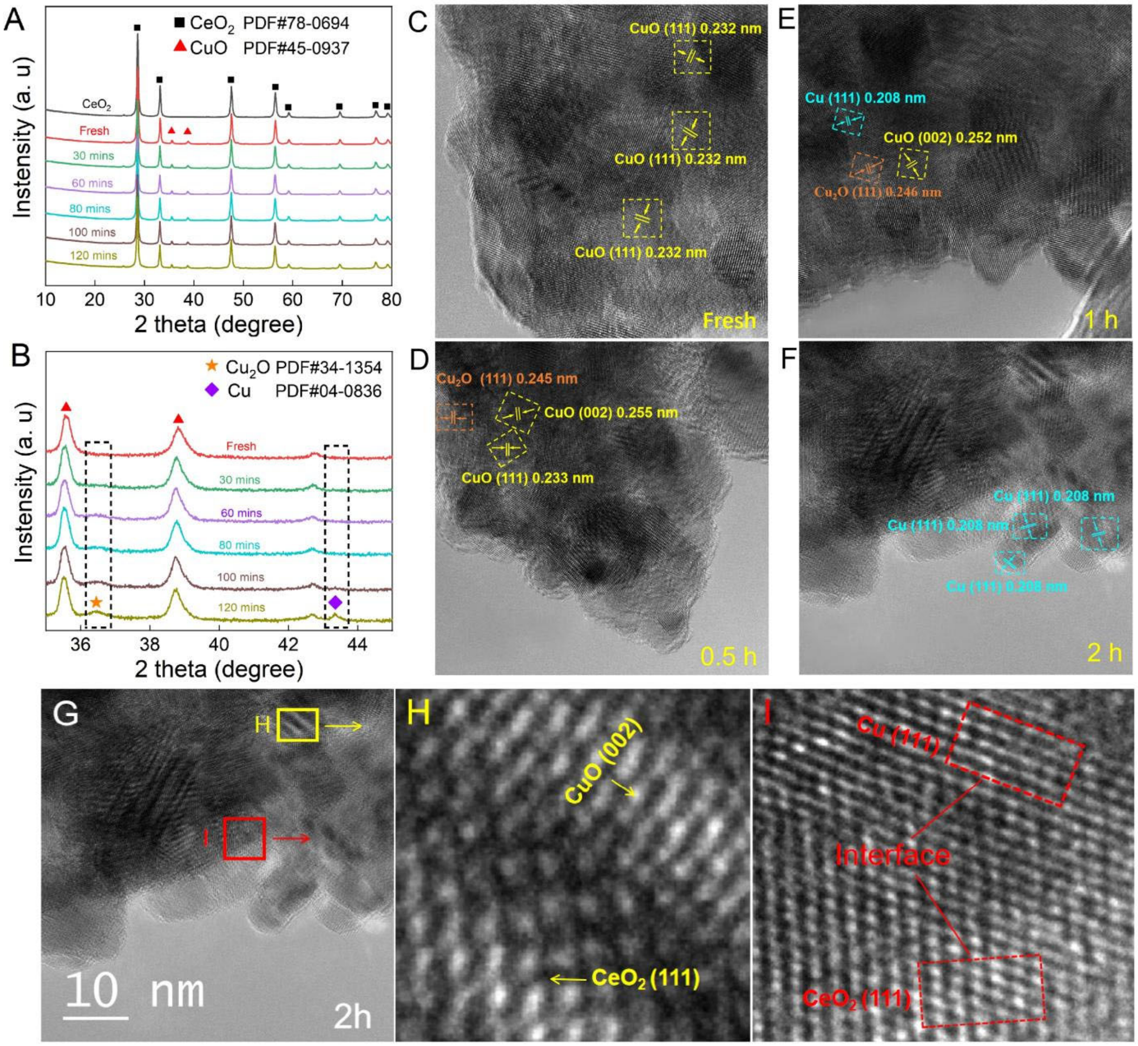

Figure 2. XRD patterns of the fresh and spent CuO/CeO$_2$ catalysts (10 wt.% loading) at different reaction times, as well as of CeO$_2$ (A), and local magnification of the XRD patterns, to show the appearance of Cu$_2$O and Cu species after 120 mins reaction time (B); Representative HRTEM images of fresh CuO/CeO$_2$ catalyst (C), and spent CuO/CeO$_2$ catalysts after 0.5 h (D), 1 h (E), and 2 h (F).The boundary area formed between copper oxide species and ceria in HRTEM (G-I).

Figure 3 shows the Cu 2p spectra of the fresh and spent CuO/CeO$_2$ catalysts (after 0.5, 1 and 2 h), in which Cu 2p$^{3/2}$ and Cu 2p$^{1/2}$ signals with two satellite peaks are observed after deconvolution. The peaks with binding energy of 934.3 and 954.3 eV are caused by Cu^{2+} species, and the peak with binding energy of 952.0 eV is ascribed to Cu^{+} species. It can be seen that the peak of Cu^{+} increases gradually during the induction period, but its intensity is still much lower than that of Cu^{2+}, even for the spent sample after 2 h reaction. Moreover, Cu 2p$^{3/2}$ peak shift towards lower binding energy with increasing reaction time, indicating a reduction reaction. These results indicate that a part of the CuO species were gradually reduced to form Cu^{+}/Cu^{0} species.In addition, the UV-vis spectra, illustrated in Figure S13, also demonstrate more Cu^{+} in the spent catalysts. Figure 3B depicts the Ce 3d spectra, in which Ce^{3+} (881.6 eV, 887.7 eV, 898.0 eV, and 903.1 eV) and Ce^{4+} (884.1 eV, 890.2 eV, 900.0 eV, 902.1 eV, 908.0 eV, and 917.6 eV) species can be distinguished after deconvolution. Clearly, the intensity of the Ce^{3+} peaks (881.6 eV, 887.7 eV, 898.0 eV, and 903.1 eV) gradually rises in the induction period. The calculated ratio of Ce^{3+}/ (Ce^{3+} + Ce^{4+}) from the XPS spectra is presented in Table S4-7, in which the content of Ce^{3+} increases from 4.8 % (fresh sample) to 18.8 % (spent after 2 h), suggesting more oxygen vacancies (O_v) in the spent catalysts.[49] Figure 3C presents the O 1s spectra, in which two peaks can be distinguished after deconvolution. The peak at low binding energy is usually ascribed to lattice oxygen (O_{latt}) species, and the peak at relative high binding energy is generally caused by oxygen vacancies (O_v, which can also be called surface-adsorbed oxygen (O_{ad}), since O_v can combine with oxygen to from O_{ad} when the catalyst is exposed to gas that contains oxygen).[50] The peak areas of O_{latt} and O_v have been integrated, and thus the relative content can be calculated. As shown in Table S4-7, the relative content of O_v (indicated by $O_v/(O_v+O_{latt})$) for the samples gradually rises in the order of Fresh < 0.5 h < 1 h < 2 h, while the relative content of O_{latt} exhibits the opposite trend. That is, as the induction period progresses, the content of O_v in the CuO/CeO_2 catalyst gradually increases, and the spent CuO/CeO_2 catalyst after 2 h reaction exhibits the highest content of O_v. The O_{latt} in Cu-O-Ce species can be consumed by H species during the reaction process, as shown in Eq. (1). The concentration increase of Cu-O-Ce species in CuO/CeO_2 catalyst should be due to the intrinsic $Ce^{3+} - \square - Cu^{+}$in CuO/CeO_2 catalyst. The presence of the Ce^{3+} and Cu^{+} in the initial CuO/CeO_2 catalyst is well established.[40]

$$Ce^{4+} - O^{2-} - Cu^{2+} + xH \rightarrow Ce^{3+} - \square - Cu^{+} + H_2 \qquad (3)$$

Hence, the presence of Ce^{3+} was assigned with the generation of O_v according to the charge compensation,[51, 52] which should be ascribed to the formation of Cu–O–Ce species according to Ayatusy's work.[53] Thus, it is reasonable to infer from the increasing atomic ratio of $Ce^{3+}/Ce^{3+}+Ce^{4+}$ over CuO/CeO_2-*x*h that the largest amounts of Cu–O–Ce species were formed in the CuO/CeO_2-*x*h catalyst.[54-56] Moreover, for the Cu-Ce system, the evolution of O_v was also related to the formation of Cu-O-Ce species.[54-56] Liu and Flytzani-Stephanopoulos[57] have also proposed that Cu^{+} species resulted from the strong interaction of a copper oxide cluster with cerium oxide. The formation of Cu^{+} might be induced by the substitution between the two oxide phases at the interface, because of the similarity of the Ce^{4+} and Cu^{+} ionic radii. The presence of large quantities of the Cu^{+} species in the CuO/CeO_2-2h catalyst suggests a synergistic interaction among Cu-O and Ce-O. This interfacial metal oxide-support synergistic effect may be the reason for the formation of Cu^{+} and Cu^{0} in the CuO/CeO_2-*x*h catalyst. In addition, it is known that Cu^{+} can enter the CeO_2 lattice to form Cu-O-Ce species. So we can deduce that the Cu^{+} is dissolved in the CeO_2 lattice and a Cu-O-Ce species was formed in CuO/CeO_2, which is consistent with the Raman results.[58] Combining the above-mentioned Cu 2p, Ce 3d and O 1s spectra, as well as the XRD patterns and HRTEM images, we can confirm that during the induction period, CuO is partially reduced to Cu^{+} or Cu^{0}. The formation of Cu^{+} is usually accompanied by the generation of Ce^{3+} and oxygen vacancies (O_v), where O_v can better anchor Cu^{+}, forming a stable Cu^{+}-Ov-Ce^{3+} species. Therefore, only a portion of the CuO is reduced to Cu^{+}/Cu^{0}, which then combines with CeO_2 to form Cu-O-Ce species. Hence, under CH_4 plasma treatment, the CuO/CeO_2 catalyst generates Cu^{+}, Ce^{3+}, and O_v at the CuO-CeO_2

interface, forming a Cu^+-O_V-Ce^{3+} species.

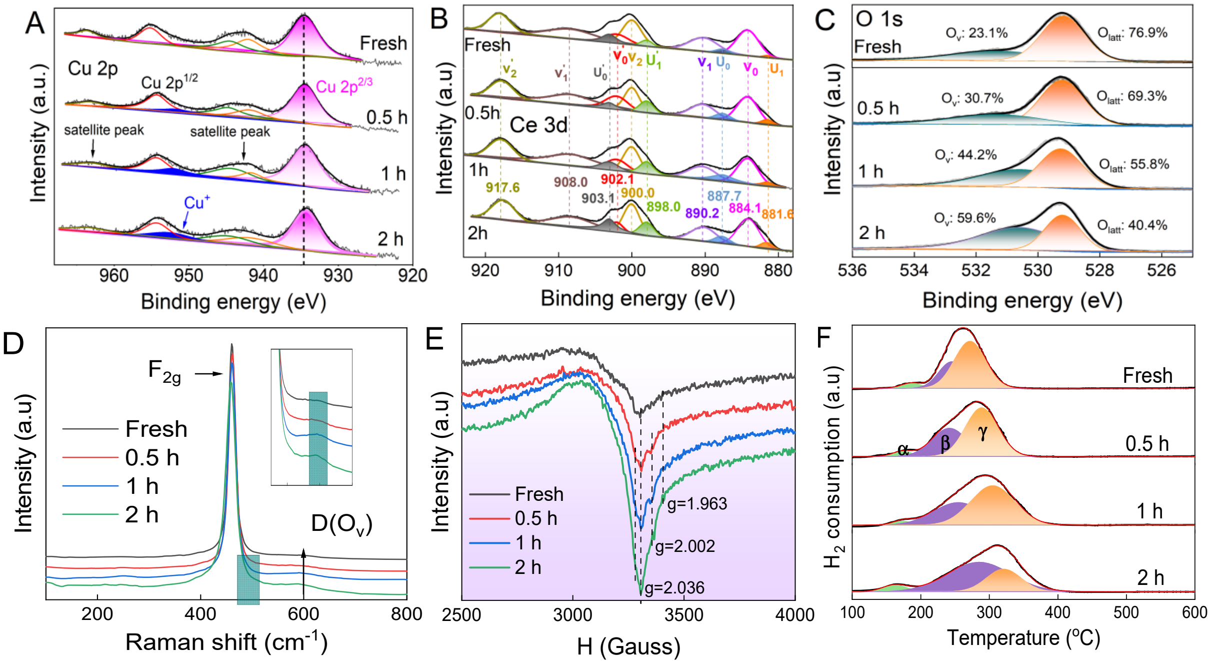

Figure 3. Characterization of the fresh and spent CuO/CeO_2 catalysts. (A) Cu 2p, (B) Ce 3d, (C) O1s, (D) Raman spectra, (E) EPR spectra, and (F) H_2-TPR profiles. The label of fresh, 0.5 h, 1 h, and 2 h mean the catalyst after 0 h, 0.5 h, 1h, and 2h of reaction, respectively.

As shown in Figure 3D, the Raman spectra exhibit a strong band at 460 cm^{-1}, corresponding to the F_{2g} Raman vibration model of the fluorite CeO_2 lattice.[59] The F_{2g} band slightly shifts from 462 cm^{-1} to 458 cm^{-1} (Figure S14), which can be ascribed to the doping of CuO species, forming Cu^+-O_V-Ce^{3+} sites. This results in the extension of the Ce−O bond lengths in the interface, and finally leads to low-energy shifts in the Raman spectra.[60, 61] The band at 580~620 cm^{-1} (D mode peak) is usually attributed to the presence of O_V. The ratio of the D band intensity to the F_{2g} band intensity (I_D/I_{F2g}) for the samples, as shown in Table S4, gradually rises in the order of Fresh < 0.5 h < 1 h < 2 h, indicating the increased concentration of O_V in the catalysts as the reaction progresses.[62] As shown in Figure 3E, the EPR spectra further demonstrate the co-existence of O_V ($g = 2.002$), Ce^{3+} ($g = 1.963$) and isolated Cu ions ($g = 2.036$),[63, 64] which further confirms the formation of Cu^+-O_V-Ce^{3+} sites on the spent CuO/CeO_2 catalysts. This can be further proven by H_2-TPR profiles of the fresh and spent CuO/CeO_2 catalysts, as shown in Figure 3F. Pure CeO_2 typically exhibits two reduction peaks at approximately 493 °C and 806 °C, which correspond to the reduction of surface and bulk oxygen in CeO_2, respectively.[65] Therefore, Figure 3F excludes the peaks for pure CeO_2. For the Cu-Ce system, a specific CuO/CeO_2 catalyst generally shows three reduction peaks,[48, 66, 67] which correspond to different Cu species. The α peak is caused by reduction of highly dispersed CuO_x clusters. The β peak corresponds to reduction of Cu-O-Ce interfacial sites. The γ peak is ascribed to reduction of crystalline CuO species and reduction of the CeO_2 surface.[68] The β peak rises during the induction period, which means that more and more Cu-O-Ce interfacial sites are formed. In addition, the β peak shifts to a higher temperature over reaction time, indicating a stronger interaction between the CuO_x species and the CeO_2 support.[23] It is worth noting that the composition of the catalyst, the concentration of its components, and the preparation method all influence the reduction temperature and the amount of H_2 consumed. Consequently, it is not possible to directly relate a certain temperature in a TPR profile to a particular chemical species on a solid.[40, 48, 55, 61, 62, 69-71]

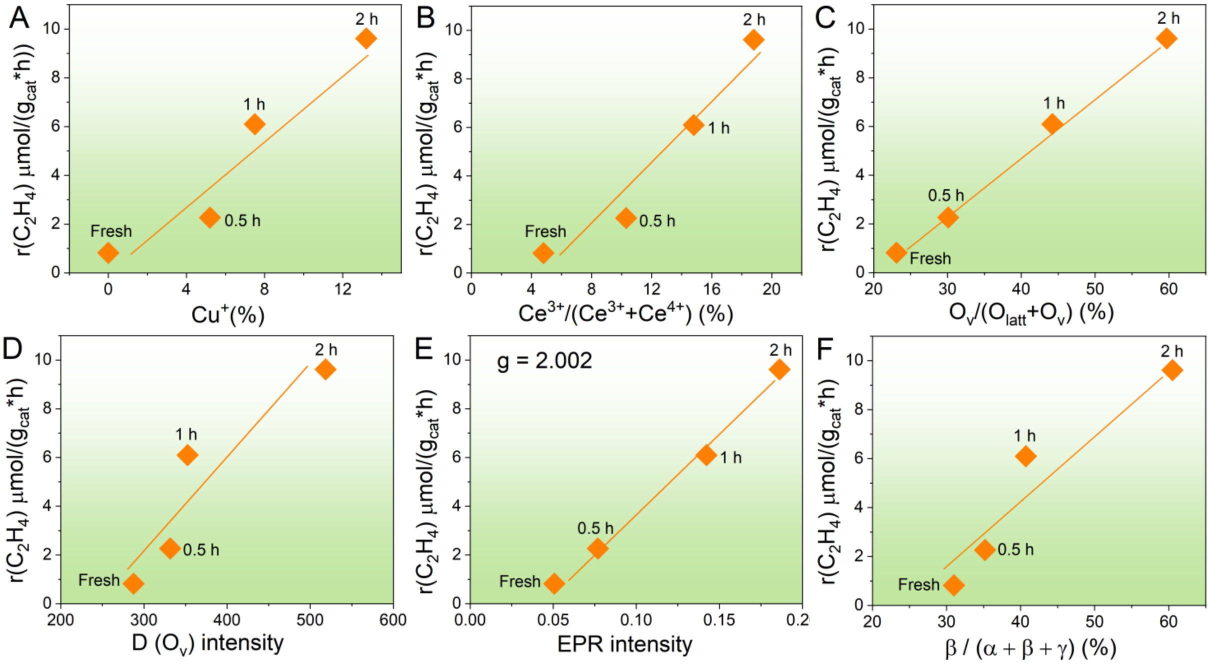

Figure 4. Relationships between the C_2H_4 synthesis rate ($r(C_2H_4)$) and the fraction of various surface species. (A) Cu^+ (obtained from XPS), (B) Ce^{3+} (from XPS), (C) O_v (from XPS), (D) O_v (from Raman), (E) O_v (from EPR), (F) Cu-O-Ce interfacial species (from H_2-TPR). The label of fresh, 0.5 h, 1 h, and 2 h mean the catalyst after 0 h, 0.5 h, 1 h, and 2 h of reaction, respectively.

We also quantitatively analyzed the relationship between the C_2H_4 synthesis rate and the fraction of the various species on the CuO/CeO_2 catalyst. As shown in Figure 4, the C_2H_4 synthesis rate is proportional to the fraction of Cu^+ (obtained from XPS), Ce^{3+} (also from XPS), O_v (obtained from XPS, Raman and EPR) and Cu-O-Ce interfacial species (from H_2-TPR), which indicates that the Cu^+-O_v-Ce^{3+} species formed in the induction period should be closely related with the CH_4 conversion into C_2H_4. In addition, we measured the C 1s spectra of the spent CuO/CeO_2 catalyst after 2 h reaction, as shown in Figure S15. Notably, there is only a graphitic carbon peak (284.8 eV) and oxidized carbon species (288.7 eV) on the catalyst surface without any carbide peak,[72, 73] which indicates that the gradual increase of the C_2H_4 synthesis rate during the induction period is not related with copper carbide or cerium carbide. Furthermore, we also investigated the performance of plasma-catalytic NOCM on CuO/SiO_2 and CuO/Al_2O_3 catalysts, as shown in Figure S16. In these cases, there was no induction period, and the C_2H_4 selectivity is as low as 5 %, indicating that CuO without assistance of CeO_2 cannot selectively catalyze the CH_4 conversion to C_2H_4. Moreover, the “Plasna+CuO” was also be investigated in Figure S17. That is, both CuO and CeO_2 are necessary to construct the active sites, i.e., Cu^+-O_v-Ce^{3+}, for the CH_4 conversion to C_2H_4.

Thirdly, we employed *in-situ* Fourier transform infrared (FTIR) spectroscopy to investigate the evolution of the plasma-catalytic NOCM on the CuO/CeO_2 catalyst during the induction period. In Figure 5A, the bands at 2800-3000 cm^{-1} correspond to the stretching vibration of the C–H bonds (CH_3^*, CH_2^* and CH^*) adsorbed on the CuO/CeO_2 catalyst.[74] The peaks of the gas-phase CH_4 can be found at 3015 cm^{-1} and 1302 cm^{-1} (Figure S18).[75] The bands at 1300–1500 cm^{-1} are generally related with the bending vibration of the C–H bonds. Specifically, the peaks at1378 cm^{-1} and 1465 cm^{-1} are due to the C–H bending vibration of CH_3^* groups. The peak at 1687 cm^{-1} is usually assigned to the stretching vibration of the C=C bond,[76, 77] and the intensity gradually increases, which indicates the gradually increased production of CH_2=CH_2 during the induction period. To clarify the intensities of the FTIR signal (2900-3050 cm^{-1}) during the induction period, we divided the spectra into four groups (Stage 1, Stage 2, Stage 3, and Stage 4) over the plasma treatment time, as shown in Figure 5(B-E). In Stage 1 (0-9 min, Figure 5B), the asymmetric C-H stretching band of CH_3^* (2960 cm^{-1}) is visible after 2 mins, due to the C_2H_6 formation. In Stage 2 (10-19 min, Figure 5C), a very narrow band (2932 cm^{-1}) emerges, corresponding to the asymmetric C-H stretching band of CH_2^*, which is lower than that of CH_3^*. In Stage 3 (20-28 min, Figure 5D), the intensity of the CH_2^* band gradually increases, while the CH_3^* band drops with prolonged plasma treatment time, even though the intensity of CH_2^* is still lower than that of CH_3^*. In Stage 4 (Figure 5E), i.e., after 28 mins of plasma ignition, the intensity of the CH_2^* characteristic peak increases continuously and surpasses the intensity of CH_3^*. The dynamic changes of CH_3^* and CH_2^* peaks over time imply the formation of Cu^+-O_v-Ce^{3+} active sites on the CuO/CeO_2 catalyst during the induction period. The Cu^+-O_v-Ce^{3+} interface sites are capable of promoting dehydrogenation of CH_3^* (from CH_4 plasma) to produce CH_2^* on the catalyst surface, which possibly speeds up plasma-catalytic NOCM for C_2H_4 generation. *In-situ* FTIR results indicate that the peak at 2932 cm^{-1} corresponds to the C-H stretching vibrations of the methylene group (CH_2^*) of alkanes. This peak mainly arises from CH_2^* formed by the dehydrogenation of CH_3^* or from $C_2H_5^*$. The peak at 2960 corresponds to the C-H stretching vibrations of alkane CH_3^* groups, primarily originating from CH_3^* or $C_2H_5^*$. Because the intensity of the 2960 cm^{-1} peak decreases, the concentration of CH_3^* or $C_2H_5^*$ also decreases. Therefore, the increase in CH_2^* intensity can only be attributed to CH_2^* formed by the dehydrogenation of CH_3^* rather than $C_2H_5^*$. Hence, the formation of C_2H_4 from the dehydrogenation of $C_2H_5^*$ can be ruled out (Figure S19B). Moreover, there was no significant vinyl (=C-H) vibration peak or changes observed at 3075-3095 cm^{-1} in the *in-situ* FTIR spectra, thus the formation of C_2H_4 from the hydrogenation of $C_2H_3^*$ can also be excluded.

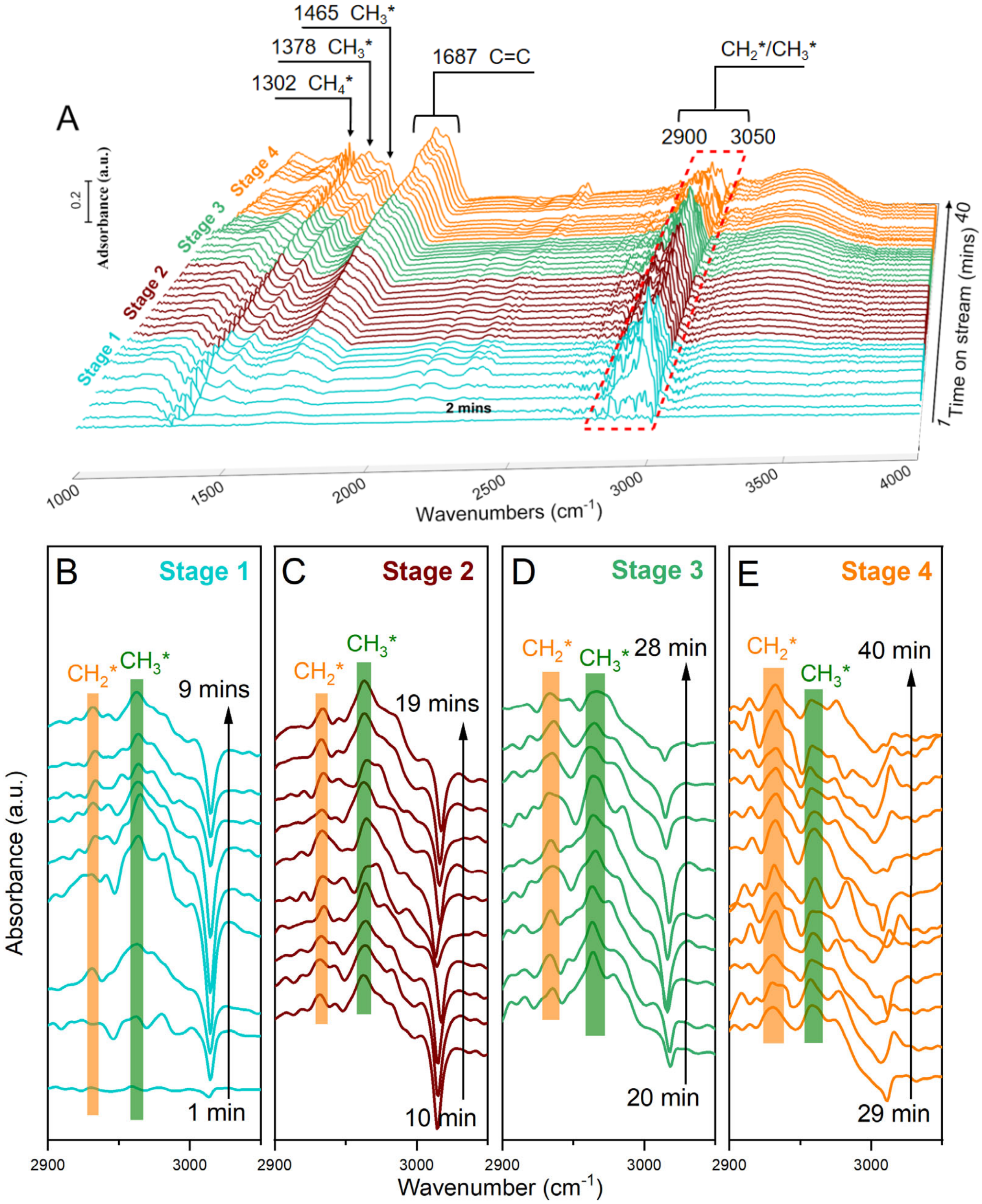

Figure 5. *In-situ* FTIR spectra. (A) Variation of the entire spectrum in the range 1000-4000 cm^{-1} with time on stream, to highlight the evolution of surface-adsorbed intermediates during the induction period, and locally enlarged spectra at 2900-3050 cm^{-1}, during (B) stage 1 (1-9 min), (C) stage 2 (10-19 min), (D) stage 3 (20-28 min) and (E) stage 4 (29-40 min).

In summary, in the plasma gas phase, the primary product is C_2H_6, which is generated by the coupling of $CH_3\cdot$ radicals originating from electron impact dissociation of CH_4. Although the pathway for C_2H_6 gradual dehydrogenation into C_2H_4 exists (Figure S8), it is not the main route for C_2H_4 formation (Figure S20). In contrast, it was observed by the *in-situ* FTIR that C1 species (CH_2^*) are adsorbed on the catalyst surface before forming higher hydrocarbons. As the reaction progresses, the intensity of CH_2^* gradually increases, along with an increase in C_2H_4 selectivity, which directly proves that C1 species couple on the catalyst surface to form C_2H_4 at the active sites of the catalyst.

In addition, the CH_2^* intensity and the rate of C_2H_4 production over time were plotted in Figure S21. The results show that at low intensities of CH_2^*, the rate of C_2H_4 production is also low. As the intensity of CH_2^* increases, the rate of C_2H_4 formation correspondingly escalates. This trend can be hypothesized to stem from the initial absence of Cu-O-Ce interface sites, which are crucial for the adsorption and subsequent dehydrogenation of CH_3^* to CH_2^*. As the reaction progresses, the concentration of Cu-O-Ce interface sites increases, enhancing the catalyst's capacity to adsorb CH_3^*. This results in a higher conversion of adsorbed CH_3^* to CH_2^* on the catalyst surface, thereby increasing the production of C_2H_4 through CH_2^* coupling. Consequently, the selectivity towards C_2H_4 gradually improves as the reaction proceeds. It is noteworthy that during the *in-situ* FTIR characterization, a catalyst wafer (0.05 g, 8 mm diameter) is employed, and thus, the interactions between plasma species and the catalyst are enhanced since it is easier for the plasma species to arrive at the catalyst surface, as opposed to a packed bed. Consequently, the induction period (ca. 0.5 h) is much shorter than observed in the fixed bed reactor (ca. 2 h).

As evidenced by the above characterization results, the Cu^+-O_v-Ce^{3+} interface sites formed by reduction of CuO/CeO_2 catalyst are favorable for CH_4 conversion to C_2H_4. However, some Cu^0 species have also been produced in the induction period (Figure 2E, 2 F and 3A), and the role of Cu^0 species in plasma-catalytic NOCM is still unclear.

To elucidate the role of these Cu^0 species, we pre-reduced the fresh CuO/CeO_2 catalyst to obtain a metallic catalyst, in which Cu-O_v-Ce active sites can be formed through reduction. We tested the Cu/CeO_2 catalyst in plasma-catalytic NOCM, as shown in Figure S22. The Cu/CeO_2 catalyst displays a somewhat better performance (6.7 % CH_4 conversion and 40 % C_2H_4 selectivity, obtained after 100 mins) than the CuO/CeO_2 catalyst (6.2 % CH_4 conversion and 36.1 % C_2H_4 selectivity, obtained after 115 mins). This means that deep reduction of CuO/CeO_2 may produce more Cu-O_v-Ce active sites, which promotes plasma-catalytic NOCM to C_2H_4. Notably, there is however still an induction period for the metallic Cu/CeO_2 catalyst. As the XRD patterns in Figure S23 show that the Cu/CeO_2 catalyst contains only metallic Cu^0 species, and has no Cu_2O or CuO species, indicating a complete reduction, we can conclude from the low selectivity of C_2H_4 in the initial stage that metallic Cu^0 is not the active species for C_2H_4 generation. However, some Cu_2O species were observed in the spent Cu/CeO_2 catalyst, which may be caused by oxygen transfer from CeO_2 to metallic Cu^0 during the reaction process. That is, some metallic Cu^0 species are transformed into Cu_2O (Cu^+) species during the induction period of Cu/CeO_2 catalyst for plasma-catalytic NOCM, explaining the rise in C_2H_4 selectivity. These results thus further demonstrate that Cu^+ species on CeO_2 surface, i.e., the Cu^+-O_v-Ce^{3+} interfacial sites, are necessary to realize plasma-catalytic NOCM for C_2H_4 production. In Figure S24, compared to the fresh CuO/CeO_2 catalyst, the relative intensity of the β peak of the pre-reduced Cu/CeO_2 catalyst increases obviously, indicating the formation of more Cu-O-Ce interfacial sites. Furthermore, compared to the fresh Cu/CeO_2 catalyst, the β peak for the spent Cu/CeO_2 catalyst not only increases but also shifts to a higher temperature. This suggests that more Cu-O-Ce species are formed after CH_4 plasma treatment, along with a stronger interaction between the CuO_x species and the CeO_2 support. In summary, after the H_2 pre-reduction treatment, more Cu-O-Ce interfacial sites have be created. Furthermore, CH_4 plasma treatment enhanced the Cu-O-Ce interaction and leads to more Cu^+-O_v-Ce^{3+} active sites.

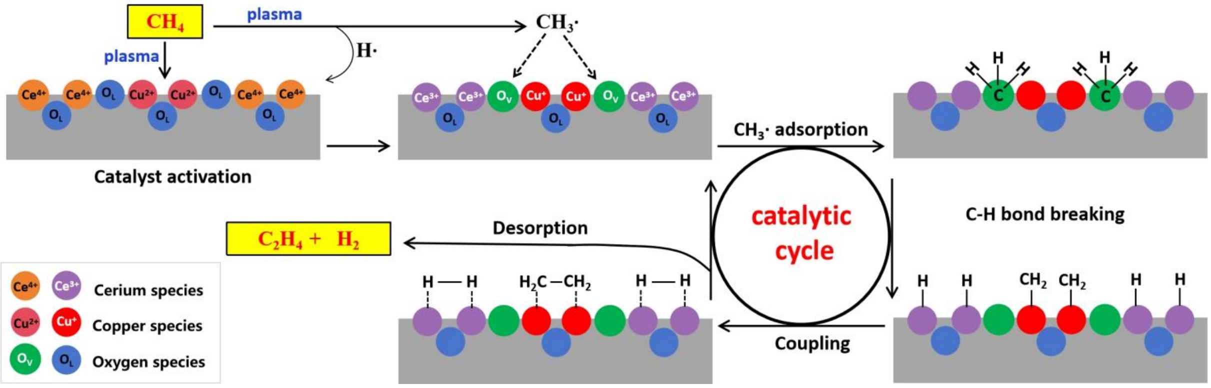

Scheme 1. Plausible reaction mechanisms of plasma-catalytic non-oxidative coupling of methane to ethylene and hydrogen on Cu^+-O_v-Ce^{3+} interfacial sites (O_L: lattice oxygen; O_v: oxygen vacancy).

Possible reaction pathways involved in the non-oxidative coupling of CH_4 to C_2H_4 are illustrated in Scheme 1. Firstly, CH_4 dissociates in the gas phase through inelastic collisions with plasma energetic electrons ($CH_4 + e \rightarrow CH_3 \cdot + H \cdot + e$). The C atom in $CH_3\cdot$ has an unpaired electron, giving it a tendency to form coordination bonds with coordinatively unsaturated metal ions. The reducibility of CeO_2 and CuO lead to the formation of oxygen vacancies (O_V) at the CuO-CeO_2 interface, resulting in the formation of Cu^+-O_v-Ce^{3+} structure. The O_v provides adsorption sites for $CH_3\cdot$, and the coordinatively unsaturated Cu^+ and Ce^{3+} can strongly coordinate with $CH_3\cdot$, facilitating the cleavage of C-H bonds to produce adsorbed CH_2* and H* species. Hence, during the induction period, CuO/CeO_2 is partially reduced and modified by hydrogen species in the plasma, forming Cu^+-O_v-Ce^{3+} species. Subsequently, an increasing number of $CH_3\cdot$ radicals are adsorbed at the Cu^+-O_v-Ce^{3+} interfacial sites, where dehydrogenation occurs, leading to the formation of adsorbed CH_2*. As the adsorbed CH_2* species accumulate, coupling reactions occur between each other, resulting in the production of C_2H_4. Additionally, Cu sites helps weaken the adsorption strength of C_2H_4, promoting its desorption. Therefore, during the induction period, the quantity of Cu^+-O_v-Ce^{3+} species increases, enhancing both the selectivity and production rate of C_2H_4.

Conclusion

We studied one-step non-oxidative coupling of methane (CH_4) to ethylene (C_2H_4) at atmospheric pressure and mild temperature (ca. 180-190 ºC), by a combination of non-thermal plasma and a CuO_x/CeO_2 catalyst, achieving 36.1% C_2H_4 selectivity and 6.2% CH_4 conversion, and even slightly higher (40 % C_2H_4 selectivity and 6.7% CH_4 conversion) when using a Cu/CeO_2 catalyst. Interestingly, we observed an induction period for the fresh CuO/CeO_2 catalyst (as well as for the Cu/CeO_2 catalyst) with gradually increased C_2H_4 selectivity. Characterization of the spent catalysts indicates that the CuO/CeO_2 catalyst is partially reduced to generate Cu^+, Ce^{3+} and O_v species, which accompany the formation of Cu^+-O_v-Ce^{3+} sites. In addition, the C_2H_4 selectivity is proportional to the fraction of Cu^+, Ce^{3+}, O_v and Cu-O-Ce interfacial species, which indicates that Cu^+-O_v-Ce^{3+} is the active site for non-oxidative coupling of CH_4 to C_2H_4. Combination of our *in-situ* FTIR results and catalyst characterization indicates that Cu^+-O_v-Ce^{3+} interface sites are capable of promoting dehydrogenation of CH_3^* (from CH_4 plasma) to produce CH_2^* on the catalyst surface, which speeds up the NOCM for C_2H_4 production. Our work not only sheds light to the design of efficient catalysts for NOCM to C_2H_4, but also provides new insights into the dynamic evolution of a catalyst during plasma treatment, which is critical to understand the development of hybrid plasma-catalytic systems toward practical applications.

Data availability

The data that support the plots and findings in this paper are available from the corresponding author upon reasonable request.

Acknowledgments

This work was supported by the National Natural Science Foundation of China [22472018]. The China Scholarship Council is gratefully acknowledged. The instrumental analysis center of Dalian University of Technology is also gratefully acknowledged.

References

(1) Xie, P.; Pu, T.; Nie, A.; Hwang, S.; Purdy, S. C.; Yu, W.; Su, D.; Miller, J. T.; Wang, C. Nanoceria-Supported Single-Atom Platinum Catalysts for Direct Methane Conversion. *Acs Catalysis* **2018**, *8* (5), 4044-4048. DOI: 10.1021/acscatal.8b00004.

(2) Tang, C.; Du, S.; Huang, H.; Tan, S.; Zhao, J.; Zhang, H.; Ni, W.; Yue, X.; Ding, Z.; Zhang, Z.; et al. Au–Pd Tandem Photocatalysis for Nonoxidative Coupling of Methane toward Ethylene. *ACS Catalysis* **2023**, *13* (10), 6683-6689. DOI: 10.1021/acscatal.3c00507.

(3) Gerceker, D.; Motagamwala, A. H.; Rivera-Dones, K. R.; Miller, J. B.; Huber, G. W.; Mavrikakis, M.; Dumesic, J. A. Methane Conversion to Ethylene and Aromatics on PtSn Catalysts. *Acs Catalysis* **2017**, *7* (3), 2088-2100. DOI: 10.1021/acscatal.6b02724.

(4) Liu, Z.; Ho Li, J. P.; Vovk, E.; Zhu, Y.; Li, S.; Wang, S.; van Bavel, A. P.; Yang, Y. Online Kinetics Study of Oxidative Coupling of Methane over La2O3 for Methane Activation: What Is Behind the Distinguished Light-off Temperatures? *ACS Catalysis* **2018**, *8* (12), 11761-11772. DOI: 10.1021/acscatal.8b03102.

(5) Luo, L.; You, R.; Liu, Y.; Yang, J.; Zhu, Y.; Wen, W.; Pan, Y.; Qi, F.; Huang, W. Gas-Phase Reaction Network of Li/MgO-Catalyzed Oxidative Coupling of Methane and Oxidative Dehydrogenation of Ethane. *ACS Catalysis* **2019**, *9* (3), 2514-2520. DOI: 10.1021/acscatal.8b04728.

(6) Qian, K.; You, R.; Guan, Y.; Wen, W.; Tian, Y.; Pan, Y.; Huang, W. Single-Site Catalysis of Li-MgO Catalysts for Oxidative Coupling of Methane Reaction. *ACS Catalysis* **2020**, *10* (24), 15142-15148. DOI: 10.1021/acscatal.0c03896.

(7) Kiani, D.; Sourav, S.; Baltrusaitis, J.; Wachs, I. E. Elucidating the Effects of Mn Promotion on SiO2-Supported Na-Promoted Tungsten Oxide Catalysts for Oxidative Coupling of Methane (OCM). *ACS Catalysis* **2021**, *11* (16),

10131-10137. DOI: 10.1021/acscatal.1c01392.

(8) Ishioka, S.; Fujiwara, A.; Nakanowatari, S.; Takahashi, L.; Taniike, T.; Takahashi, K. Designing Catalyst Descriptors for Machine Learning in Oxidative Coupling of Methane. *ACS Catalysis* **2022**, *12* (19), 11541-11546. DOI: 10.1021/acscatal.2c03142.

(9) Wang, H.; Schmack, R.; Sokolov, S.; Kondratenko, E. V.; Mazheika, A.; Kraehnert, R. Oxide-Supported Carbonates Reveal a Unique Descriptor for Catalytic Performance in the Oxidative Coupling of Methane (OCM). *ACS Catalysis* **2022**, *12* (15), 9325-9338. DOI: 10.1021/acscatal.1c05177.

(10) Guo, X.; Fang, G.; Li, G.; Ma, H.; Fan, H.; Yu, L.; Ma, C.; Wu, X.; Deng, D.; Wei, M.; et al. Direct, Nonoxidative Conversion of Methane to Ethylene, Aromatics, and Hydrogen. *Science* **2014**, *344*, 616-619.

(11) Sakbodin, M.; Wu, Y.; Oh, S. C.; Wachsman, E. D.; Liu, D. Hydrogen-Permeable Tubular Membrane Reactor: Promoting Conversion and Product Selectivity for Non-Oxidative Activation of Methane over an Fe(c)SiO(2) Catalyst. *Angew Chem Int Ed Engl* **2016**, *55* (52), 16149-16152. DOI: 10.1002/anie.201609991 From NLM PubMed-not-MEDLINE.

(12) Han, S. J.; Lee, S. W.; Kim, H. W.; Kim, S. K.; Kim, Y. T. Nonoxidative Direct Conversion of Methane on Silica-Based Iron Catalysts: Effect of Catalytic Surface. *Acs Catalysis* **2019**, *9* (9), 7984-7997. DOI: 10.1021/acscatal.9b01643.

(13) Jiang. W,; Zhang. J.; Guo. H, Sulfite activation by non-thermal plasma coupled with Fe^{2+} for ibuprofen degradation: In-depth insight into activation energy barrier and mechanism, *Separation and Purification Technology*, **2024**, 351, 128042.

(14) Wang. Y,; Xiang. L,; Li. Z,; Han. J.; Guo. H, Sulfite activation by water film dielectric barrier discharge plasma for ibuprofen degradation: efficiency, comparison of persulfate, mechanism, active substances dominant to pathway, and toxicity evaluation, *Separation and Purification Technology*, **2024**, 330, 125531.

(15) Mamoru Okumoto, A. M. Conversion of methane for higher hydrocarbon fuel synthesis using pulsed discharge plasma method. *Catalysis Today* **2001**, *71*, 211-217.

(16) Kogelschatz, U. Dielectric-barrier Discharges: Their History, Discharge Physics, and Industrial Applications. *Plasma Chemistry and Plasma Processing* **2003**, *23*, 1-45.

(17) Huang, J; Han, J; Guo, H. Fe^{2+}/Fe^{3+} cycle promoting hydroxylamine activation in dielectric barrier discharge system for efficient degradation of antibiotics: Insight into performance and activation mechanism, *Separation and Purification Technology*, 2025, 355, 129709.

(18) Gallon Helen, J.; Tu, X.; Twigg Martyn, V.; Whitehead J, C. Plasma-assisted methane reduction of a NiO catalyst-Low temperature activation of methane and formation of carbon nanofibres. *Appl Catal B-Environ* **2011**, *106* (3-4), 616-620. DOI: 10.1016/j.apcatb.2011.06.023.

(19) Antonius Indarto, J.-W. C., Hwaung Lee, Hyung Keun Song. Kinetic Modeling of Plasma Methane Conversion Using Gliding Arc. *Journal of Natural Gas Chemistry* **2005**, *14*, 13-21.

(20) Indarto, A.; Coowanitwong, N.; Choi, J.-W.; Lee, H.; Song, H. K. Kinetic modeling of plasma methane conversion in a dielectric barrier discharge. *Fuel Processing Technology* **2008**, *89* (2), 214-219. DOI: 10.1016/j.fuproc.2007.09.006.

(21) Kettlitz, M. H. M. M. M. Mechanism of hydrocarbon formation from methane in a pulsed microwave plasma. *J. Appl. Phys.* **2002**, *92*, 7022-7031. DOI: 10.1063/1.1521518 兴.

(22) Gao, Y.; Zhang, S.; Sun, H.; Wang, R.; Tu, X.; Shao, T. Highly efficient conversion of methane using microsecond and nanosecond pulsed spark discharges. *Applied Energy* **2018**, *226*, 534-545. DOI: 10.1016/j.apenergy.2018.06.006.

(23) Hu Shuanghui, W. B., Lv Yijun,Yan Wenjuan. Conversion of Methane to C2 Hydrocarbons and Hydrogen Using a Gliding Arc Reactor. *Plasma Science and Technology* **2013**, *15*, 555-561. DOI: 10.1088/1009-0630/15/6/13.

(24) Schmidt-Szalowski, K.; Krawczyk, K.; Mlotek, M. Catalytic effects of metals on the conversion of methane in gliding discharges. *Plasma Processes and Polymers* **2007**, *4* (7-8), 728-736. DOI: 10.1002/ppap.200700052.

(25) Konno, K.; Onoe, K.; Takiguchi, Y.; Yamaguchi, T. Conversion of methane by an electric barrier-discharge plasma using an inner electrode with discharge disks set at 5 mm intervals. *Chemical Engineering Research and Design* **2015**, *95*, 144-149. DOI: 10.1016/j.cherd.2015.01.012.

(26) Kundu, S. K.; Kennedy, E. M.; Gaikwad, V. V.; Molloy, T. S.; Dlugogorski, B. Z. Experimental investigation of alumina and quartz as dielectrics for a cylindrical double dielectric barrier discharge reactor in argon diluted methane plasma. *Chemical Engineering Journal* **2012**, *180*, 178-189. DOI: 10.1016/j.cej.2011.11.039.

(27) Taheraslani, M.; Gardeniers, H. Plasma Catalytic Conversion of CH4 to Alkanes, Olefins and H2 in a Packed Bed DBD Reactor. *Processes* **2020**, *8* (7). DOI: 10.3390/pr8070774.

(28) Delikonstantis E., Scapinello M., Stefanidis Georgios D. Low energy cost conversion of methane to ethylene in a hybrid plasma-catalytic reactor system[J]. Fuel Processing Technology, 2018, 176: 33-42.

(29) Wang Kangjun L. X., Zhu Aimin. A Green Process for High-Concentration Ethylene and Hydrogen Production from Methane in a Plasma-Followed-by-Catalyst Reactor[J]. Plasma Science and Technology, 2011, 13: 77.

(30) Liu, R.; Hao, Y.; Wang, T.; Wang, L.; Bogaerts, A.; Guo, H.; Yi, Y. Hybrid plasma-thermal system for methane conversion to ethylene and hydrogen. *Chemical Engineering Journal* **2023**, *463*. DOI: 10.1016/j.cej.2023.142442.

(31) Liu, R.; Morais, E.; Li, D; Liu, P,; Chen, Q,; Li, S,; Wang, L.; Gao, X,; Bogaerts, A.; Guo, H.; Yi, Y. Hybrid plasma-thermal system for methane conversion to ethylene and hydrogen. *Chemical Engineering Journal* **2024**, 498, 155733

(32) Lina Liu, S. D., Zhikun Zhang, and Sibudjing Kawi. Nonoxidative Coupling of Methane over Ceria-Supported SingleAtom Pt Catalysts in DBD Plasma. *ACS Appl. Mater. Interfaces* **2022**, *14*, 5363-5375. DOI: 10.1021/acsami.1c21550.

(33) Jo, S.; Kim, T.; Lee Dae, H.; Kang Woo, S.; Song, Y.-H. Effect of the Electric Conductivity of a Catalyst on Methane Activation in a Dielectric Barrier Discharge Reactor. *Plasma Chemistry and Plasma Processing* **2014**, *34* (1), 175-186. DOI: 10.1007/s11090-013-9505-1.

(34) Ma, Y.; Han, X.; Xu, S.; Li, Z.; Lu, W.; An, B.; Lee, D.; Chansai, S.; Sheveleva, A. M.; Wang, Z.; et al. Direct Conversion of Methane to Ethylene and Acetylene over an Iron-Based Metal–Organic Framework. *Journal of the American Chemical Society* **2023**, *145* (38), 20792-20800. DOI: 10.1021/jacs.3c03935.

(35) Engelmann, Y.; Mehta, P.; Neyts, E. C.; Schneider, W. F.; Bogaerts, A. Predicted Influence of Plasma Activation on Nonoxidative Coupling of Methane on Transition Metal Catalysts. *ACS Sustainable Chemistry & Engineering* **2020**, *8* (15), 6043-6054. DOI: 10.1021/acssuschemeng.0c00906.

(36) Yang, Y. Direct Non-oxidative Methane Conversion by Non-thermal Plasma: Modeling Study. *Plasma Chemistry and Plasma Processing* **2003**, *23*, 327-346.

(37) Li, L.; Zhang, C.; Chen, F.; Xiang, Y.; Yan, J.; Chu, W. Facile fabrication of hollow structured Cu-Ce binary oxides and their catalytic properties for toluene combustion. *Catalysis Today* **2021**, *376*, 239-246. DOI: 10.1016/j.cattod.2020.05.038.

(38) Atribak, I.; Azambre, B.; Bueno López, A.; García-García, A. Effect of NO adsorption/desorption over ceria-zirconia catalysts on the catalytic combustion of model soot. *Applied Catalysis B: Environmental* **2009**, *92* (1-2), 126-137. DOI: 10.1016/j.apcatb.2009.07.015.

(39) Wang, L.; Peng, H.; Shi, S.-l.; Hu, Z.; Zhang, B.-z.; Ding, S.-m.; Wang, S.-h.; Chen, C. Metal-organic framework derived hollow CuO/CeO2 nano-sphere: To expose more highly dispersed Cu-O-Ce interface for enhancing preferential CO oxidation. *Appl Surf Sci* **2022**, *573*. DOI: 10.1016/j.apsusc.2021.151611.

(40) Wang, Z.; Qu, Z.; Quan, X.; Li, Z.; Wang, H.; Fan, R. Selective catalytic oxidation of ammonia to nitrogen over CuO-CeO2 mixed oxides prepared by surfactant-templated method. *Applied Catalysis B: Environmental* **2013**, *134-135*, 153-166. DOI: 10.1016/j.apcatb.2013.01.029.

(41) Xing, Y.; Wu, J.; Liu, D.; Zhang, C.; Han, J.; Wang, H.; Li, Y.; Hou, X.; Zhang, L.; Gao, Z. Different metal (Mn, Fe, Co, Ni, and Zr) decorated Cu/CeO(2) catalysts for efficient CO oxidation in a rich CO(2)/H(2) atmosphere. *Phys Chem Chem Phys* **2024**, *26* (15), 11618-11630. DOI: 10.1039/d3cp06125f From NLM PubMed-not-MEDLINE.

(42) Lu, J.; Wang, J.; Zou, Q.; Zhao, Y.; Fang, J.; He, S.; He, D.; Luo, Y. Catalytic performance of transition metals (Co, Ni, Zn, Mo) doped CuO-Ce0.8Zr0.2O2 based catalysts for CO preferential oxidation in H2-rich streams. *Journal of Alloys and Compounds* **2019**, *784*, 1248-1260. DOI: 10.1016/j.jallcom.2019.01.107.

(43) Qu, Z.; Gao, K.; Fu, Q.; Qin, Y. Low-temperature catalytic oxidation of toluene over nanocrystal-like Mn–Co

oxides prepared by two-step hydrothermal method. *Catalysis Communications* **2014**, *52*, 31-35. DOI: 10.1016/j.catcom.2014.03.035.

(44) Shan, W. Reduction property and catalytic activity of Ce1−XNiXO2 mixed oxide catalysts for CH4 oxidation. *Applied Catalysis A: General* **2003**, *246* (1), 1-9. DOI: 10.1016/s0926-860x(02)00659-2.

(45) Xiong, Y.; Li, L.; Zhang, L.; Cao, Y.; Yu, S.; Tang, C.; Dong, L. Migration of copper species in Ce(x)Cu(1-x)O(2) catalyst driven by thermal treatment and the effect on CO oxidation. *Phys Chem Chem Phys* **2017**, *19* (32), 21840-21847. DOI: 10.1039/c7cp03735j From NLM PubMed-not-MEDLINE.

(46) Wang, F.; Tian, J.; Li, M.; Li, W.; Chen, L.; Liu, X.; Li, J.; Muhetaer, A.; Li, Q.; Wang, Y.; et al. A Photoactivated Cu-CeO(2) Catalyst with Cu-[O]-Ce Active Species Designed through MOF Crystal Engineering. *Angew Chem Int Ed Engl* **2020**, *59* (21), 8203-8209. DOI: 10.1002/anie.201916049 From NLM PubMed-not-MEDLINE.

(47) Mistri, R.; Rahaman, M.; Llorca, J.; Priolkar, K. R.; Colussi, S.; Ray, B. C.; Gayen, A. Liquid phase selective oxidation of benzene over nanostructured CuxCe1−xO2−δ (0.03≤x≤0.15). *Journal of Molecular Catalysis A: Chemical* **2014**, *390*, 187-197. DOI: 10.1016/j.molcata.2014.03.024.

(48) Ye, Y.; Xu, J.; Gao, L.; Zang, S.; Chen, L.; Wang, L.; Mo, L. CuO/CeO2 catalysts prepared by modified impregnation method for ethyl acetate oxidation. *Chemical Engineering Journal* **2023**, *471*. DOI: 10.1016/j.cej.2023.144667.

(49) Wei, Y.; Zhang, Y.; Zhang, P.; Xiong, J.; Mei, X.; Yu, Q.; Zhao, Z.; Liu, J. Boosting the Removal of Diesel Soot Particles by the Optimal Exposed Crystal Facet of CeO2 in Au/CeO2 Catalysts. *Environmental Science & Technology* **2019**, *54* (3), 2002-2011. DOI: 10.1021/acs.est.9b07013.

(50) Wang, M.; Shen, M.; Jin, X.; Tian, J.; Li, M.; Zhou, Y.; Zhang, L.; Li, Y.; Shi, J. Oxygen Vacancy Generation and Stabilization in CeO2–x by Cu Introduction with Improved CO2 Photocatalytic Reduction Activity. *ACS Catalysis* **2019**, *9* (5), 4573-4581. DOI: 10.1021/acscatal.8b03975.

(51) Fan, J.; Wu, X.; Wu, X.; Liang, Q.; Ran, R.; Weng, D. Thermal ageing of Pt on low-surface-area CeO2–ZrO2–La2O3 mixed oxides: Effect on the OSC performance. *Applied Catalysis B: Environmental* **2008**, *81* (1-2), 38-48. DOI: 10.1016/j.apcatb.2007.11.022.

(52) Li, J.; Han, Y.; Zhu, Y.; Zhou, R. Purification of hydrogen from carbon monoxide for fuel cell application over modified mesoporous CuO–CeO2 catalysts. *Applied Catalysis B: Environmental* **2011**. DOI: 10.1016/j.apcatb.2011.08.010.

(53) Ayastuy, J. L.; Gurbani, A.; González-Marcos, M. P.; Gutiérrez-Ortiz, M. A. CO oxidation on CeXZr1−XO2-supported CuO catalysts: Correlation between activity and support composition. *Applied Catalysis A: General* **2010**, *387* (1-2), 119-128. DOI: 10.1016/j.apcata.2010.08.015.

(54) Zhang, X.; Wang, H.; Jiang, X.; Sun, H.; Qu, Z. Study of synergistic effect between CuO and CeO2 over CuO@CeO2 core–shell nanocomposites for NH3-SCO. *Catalysis Science & Technology* **2019**, *9* (11), 2968-2981. DOI: 10.1039/c9cy00480g.

(55) Lin, Y.; Wang, L.; Chi, J.; Peng, H.; Gao, X.; Zhang, B.; Wang, S.; Chen, C.; Zhang, N.; Hong, S. Cu-Embedded CeO2 Nanotubes as CO2–Resistant Catalysts for Preferential CO Oxidation in H2-Rich Streams. *ACS Applied Nano Materials* **2023**, *6* (24), 23477-23487. DOI: 10.1021/acsanm.3c04861.

(56) Singhania, A.; Gupta, S. M. Ce(1-x) O(2)Cu(x) Nanoparticles: Synthesis, Characterization and Catalytic Activity for Phenol Degradation. *J Nanosci Nanotechnol* **2019**, *19* (8), 5220-5226. DOI: 10.1166/jnn.2019.16825 From NLM PubMed-not-MEDLINE.

(57) Flytzani-Stephanopoulos, W. L. a. M. Total Oxidation of Carbon Monoxide and Methane over Transition Metal-Fluorite Oxide Composite Catalysts. *Journal of Catalysis* **1995**, *153*, 304-316.

(58) Chen, G.; Li, Q.; Wei, Y.; Fang, W.; Yang, Y. Low temperature CO oxidation on Ni-promoted CuO-CeO2 catalysts. *Chinese Journal of Catalysis* **2013**, *34* (2), 322-329. DOI: 10.1016/s1872-2067(11)60468-3.

(59) Xiao, M.; Zhang, X.; Yang, Y.; Cui, X.; Chen, T.; Wang, Y. M (M = Mn, Co, Cu)-CeO2 catalysts to enhance their CO catalytic oxidation at a low temperature: Synergistic effects of the interaction between Ce3+-Mx+-Ce4+ and the oxygen vacancy defects. *Fuel* **2022**, *323*. DOI: 10.1016/j.fuel.2022.124379.

(60) Wang, W.-W.; Du, P.-P.; Zou, S.-H.; He, H.-Y.; Wang, R.-X.; Jin, Z.; Shi, S.; Huang, Y.-Y.; Si, R.; Song, Q.-S.; et al.

Highly Dispersed Copper Oxide Clusters as Active Species in Copper-Ceria Catalyst for Preferential Oxidation of Carbon Monoxide. *ACS Catalysis* **2015**, *5* (4), 2088-2099. DOI: 10.1021/cs5014909.

(61) Sun, H.; Wang, H.; Qu, Z. Construction of CuO/CeO2 Catalysts via the Ceria Shape Effect for Selective Catalytic Oxidation of Ammonia. *ACS Catalysis* **2023**, *13* (2), 1077-1088. DOI: 10.1021/acscatal.2c05168.

(62) Wang, B.; Zhang, H.; Xu, W.; Li, X.; Wang, W.; Zhang, L.; Li, Y.; Peng, Z.; Yang, F.; Liu, Z. Nature of Active Sites on Cu–CeO2 Catalysts Activated by High-Temperature Thermal Aging. *ACS Catalysis* **2020**, *10* (21), 12385-12392. DOI: 10.1021/acscatal.0c03188.

(63) Kong, J.; Xiang, Z.; Li, G.; An, T. Introduce oxygen vacancies into CeO2 catalyst for enhanced coke resistance during photothermocatalytic oxidation of typical VOCs. *Applied Catalysis B: Environmental* **2020**, *269*. DOI: 10.1016/j.apcatb.2020.118755.

(64) Parthasarathi Bera, S. T. A., K. C. Patil, and M. S. Hegde. Studies on Cu/CeO2: A New NO Reduction Catalyst. *Journal of Catalysis* **1999**, *186*, 36-44.

(65) YAO, H. C. Y. A. Y. F. Y. Ceria in Automotive Exhaust Catalysts. *JOURNAL OF CATALYSIS* **1984**, *86*, 254-265.

(66) Xie, Y.; Wu, J.; Jing, G.; Zhang, H.; Zeng, S.; Tian, X.; Zou, X.; Wen, J.; Su, H.; Zhong, C.-J.; et al. Structural origin of high catalytic activity for preferential CO oxidation over CuO/CeO2 nanocatalysts with different shapes. *Applied Catalysis B: Environmental* **2018**, *239*, 665-676. DOI: 10.1016/j.apcatb.2018.08.066.

(67) Ding, J.; Geng, Z.; Li, L.; Wang, Y.; Zuo, Y.; Li, H.; Yang, M.; Li, G. Migration of cations in layered oxides for creating a highly active interface toward CO preferential oxidation. *Journal of Materials Chemistry A* **2021**, *9* (21), 12623-12635. DOI: 10.1039/d0ta11762e.

(68) Li, Y.; Hu, J.; Chen, M.; Wan, H. Promotion Effect of Cu for CO Oxidation on Ceria Supported PdxCuy Bimetallic Catalysts. *The Journal of Physical Chemistry C* **2022**, *126* (3), 1420-1425. DOI: 10.1021/acs.jpcc.1c10078.

(69) Wang, L.; Peng, H.; Shi, S.-l.; Li, S.-c.; Ding, S.-m.; Zhao, D.; Wang, S.-h.; Chen, C. Microwave non-thermal fusion of MOFs derived Cu-O-Ce interface for boosting CO preferential oxidation. *Appl Surf Sci* **2023**, *610*. DOI: 10.1016/j.apsusc.2022.155466.

(70) Liao, Y.; Liu, Z.; Li, Z.; Gao, G.; Ji, L.; Xu, H.; Huang, W.; Qu, Z.; Yan, N. The Unique CO Activation Effects for Boosting NH(3) Selective Catalytic Oxidation over CuO(x)-CeO(2). *Environ Sci Technol* **2022**, *56* (14), 10402-10411. DOI: 10.1021/acs.est.2c02612 From NLM Medline.

(71) Yu, W. Z.; Wu, M. Y.; Wang, W. W.; Jia, C. J. In Situ Generation of the Surface Oxygen Vacancies in a Copper-Ceria Catalyst for the Water-Gas Shift Reaction. *Langmuir* **2021**, *37* (35), 10499-10509. DOI: 10.1021/acs.langmuir.1c01428 From NLM PubMed-not-MEDLINE.

(72) Gubo, R.; Ren, P.; García Rodríguez, D.; Yu, X.; Zhang, T.; Wen, X.; Yang, Y.; Li, Y.-W.; Niemantsverdriet, J. W.; Weststrate, C. J. Atomistic Understanding of the Formation, Structure, and Decomposition of an Fe4C Iron Carbide Phase on a Copper Substrate. *The Journal of Physical Chemistry C* **2023**, *127* (26), 12811-12820. DOI: 10.1021/acs.jpcc.3c03134.

(73) Rodríguez, D. G.; Gleeson, M. A.; Lauritsen, J. V.; Li, Z.; Yu, X.; Hans Niemantsverdriet, J. W.; Kees-Jan Weststrate, C. J. Iron carbide formation on thin iron films grown on Cu(1 0 0): FCC iron stabilized by a stable surface carbide. *Appl Surf Sci* **2022**, *585*. DOI: 10.1016/j.apsusc.2022.152684.

(74) Scarduelli, G.; Guella, G.; Mancini, I.; Dilecce, G.; De Benedictis, S.; Tosi, P. Methane Oligomerization in a Dielectric Barrier Discharge at Atmospheric Pressure. *Plasma Processes and Polymers* **2009**, *6* (1), 27-33. DOI: 10.1002/ppap.200800096.

(75) Vakili, R.; Gholami, R.; Stere, C. E.; Chansai, S.; Chen, H.; Holmes, S. M.; Jiao, Y.; Hardacre, C.; Fan, X. Plasma-assisted catalytic dry reforming of methane (DRM) over metal-organic frameworks (MOFs)-based catalysts. *Applied Catalysis B: Environmental* **2020**, *260*. DOI: 10.1016/j.apcatb.2019.118195.

(76) Wood, J.; Alldrick, M. J.; Winterbottom, J. M.; Stitt, E. H.; Bailey, S. Diffuse reflectance infrared Fourier transform spectroscopy (DRIFTS) study of ethyne hydrogenation on Pd/Al2O3. *Catalysis Today* **2007**, *128* (1-2), 52-62. DOI: 10.1016/j.cattod.2007.04.016.

(77) Hu, N.; Yang, C.; He, L.; Guan, Q.; Miao, R. Ni–Cu/Al2O3 catalysts for the selective hydrogenation of acetylene: a study on catalytic performance and reaction mechanism. *New Journal of Chemistry* **2019**, *43* (46), 18120-18125.

Supporting Information

Plasma-driven Non-oxidative Coupling of Methane to Ethylene and Hydrogen at Mild Temperature over Cu_xO/CeO_2 Catalyst

Rui Liu,[1,] Shangkun Li,[1, 2,] Qian Chen,[1] Dongxing Li,[1] Jiasong Zhao,[1] Chuang Li,[1] Xiaoxia Gao,[3] Wenping Zhao,[4] Li Wang,[5] Chong Peng,[1] Annemie Bogaerts,[2] Hongchen Guo,[1, *] Yanhui Yi [1, *]

[1]State Key Laboratory of Fine Chemicals, Frontier Science Center for Smart Materials, School of Chemical Engineering, Dalian University of Technology, Dalian 116024, P.R. China.
[2]Research group PLASMANT, Department of Chemistry, University of Antwerp, Universiteitsplein 1, BE-2610 Wilrijk-Antwerp, Belgium.
[3]Instrumental Analysis Center, Dalian University of Technology, Dalian, 116024, P.R. China.
[4]China Tianchen Engineering Corporation, Tianjin, 300409, P.R. China.
[5]College of Environmental Sciences and Engineering, Dalian Maritime University, Dalian 116026, Liaoning, China

***Corresponding Author:** hongchenguo@163.com; yiyanhui@dlut.edu.cn

Table of content

1. Experimental section

1.1 Experimental Setup

The non-oxidative coupling of methane (NOCM) reaction was carried out in a coaxial dielectric barrier discharge (DBD) reactor at atmospheric pressure, as shown in Figure S1. The inner diameter of the quartz reactor is 6 mm. An aluminum foil is wrapped around the outer tube and acts as the ground electrode. A stainless-steel rod (2 mm diameter), placed inside the quartz reactor, was used as the high-voltage electrode. The length of the discharge zone in the reactor was 60 mm and the discharge gap was 2 mm. The catalyst was uniformly packed between the central high-voltage electrode and the ground electrode wrapped around the coaxial DBD reactor wall. Usually, in the experiment, we assume that all species can come into contact with the catalyst surface because the discharge was generated between the high-voltage electrode and the ground electrode. The bulk reaction temperature was controlled at 180 to 190 ºC (detected by a thermocouple) by adjusting the applied power. The reaction temperature was also recorded by a thermal infrared imager, i.e., Forward Looking Infrared Radar (FLIR), which demonstrate that the temperature measured by FLIR is a little bit higher (ca. 5 ºC) than that obtained by thermocouple. Typically, the flow rate of the feedstock was 20 mL/min (CH_4: Ar = 1:1), which was controlled by two gas flow controllers. A sinusoidal AC power supply (Suman, CTP-2000K) was connected to a transformer. The initial power and the frequency of the DBD plasma were fixed at 15-16 W and 14 kHz, respectively. The discharge parameters were collected by a digital phosphor oscilloscope (Tektronix, DPO 3012). The applied voltage of the plasma reactor was measured by a high-voltage probe (1000:1, P6015A, Tektronix). The voltage across the 0.1 μF capacitor was measured by a voltage probe (10:1, TPP0101, Tektronix), which was connected with the two sides of the capacitor. A current probe (Pearson 6585) was connected to the ground electrode to evaluate the current across the DBD plasma reactor. Analysis of the gas-phase reactive species was carried out by optical emission spectroscopy (OES), through the wall of the quartz tube. Emission of excited species in the range of 200-1100 nm was collected by an optical fiber. The exhaust gases were analyzed online by a mass spectrometer (MS, HIDEN DECRA) with Faraday detection mode, as well as an online gas chromatograph (GC, Tianmei GC7900), which was equipped with an FID detector and PLOT column (Al_2O_3, 50 m × 0.53 mm × 25 μm). The MS was mainly used for qualitative analysis to observe the variation of products, while the GC was mainly used to quantitatively analyze the effluent gases (CH_4, C_2H_2, C_2H_4, C_2H_6, C_3H_6, C_3H_8, i-C_4H_8, and n-C_4H_{10}). The concentration of each species was calculated using an external standard method with standard curves obtained from calibrated gas mixtures. The change of gas flow rate after the reaction was measured using a flow meter, which is needed to quantitatively analyze the gas composition, and to achieve the exact conversion (CH_4) and gaseous products selectivity, i.e, to account for gas expansion or contraction. The conversion of CH_4, and the selectivity of the gas-phase products and coke are calculated based on the following equations.[1]

$$\text{Conversion of } CH_4\ (\%) = \frac{\text{Moles of } CH_4 \text{ converted}}{\text{Moles of } CH_4 \text{ input}} \times 100\%$$

$$\text{Selectivity of } C_xH_y\ (\%) = \frac{\text{Moles of } C_xH_y \text{ produced} \times x}{\text{Moles of } CH_4 \text{ converted}} \times 100\%$$

$$\text{Selectivity of } H_2\ (\%) = \frac{\text{Moles of } H_2 \text{ produced} \times 0.5}{\text{Moles of } CH_4 \text{ converted}} \times 100\%$$

$$\text{Selectivity of coke } (\%) = 1 - \sum_{x=2}^{x=4} \text{selectivity of } C_xH_y$$

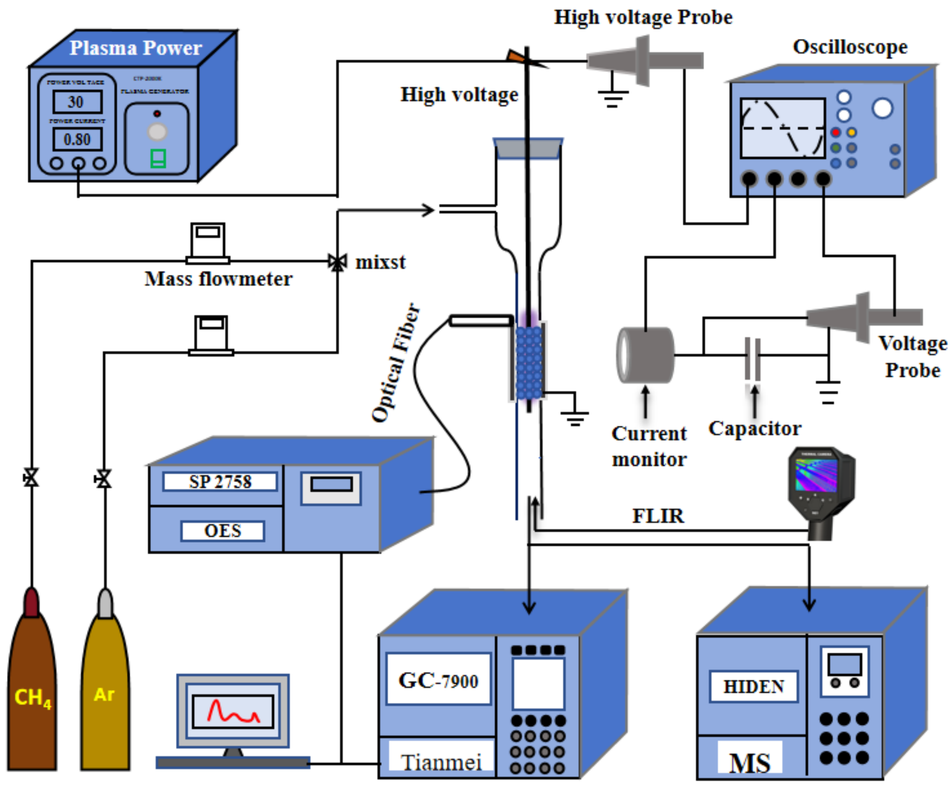

Figure S1. Schematic diagram of the experimental setup used for the plasma-catalytic non-oxidative coupling of methane to ethylene and hydrogen.

1.2 *In-Situ* FTIR Reaction Cell

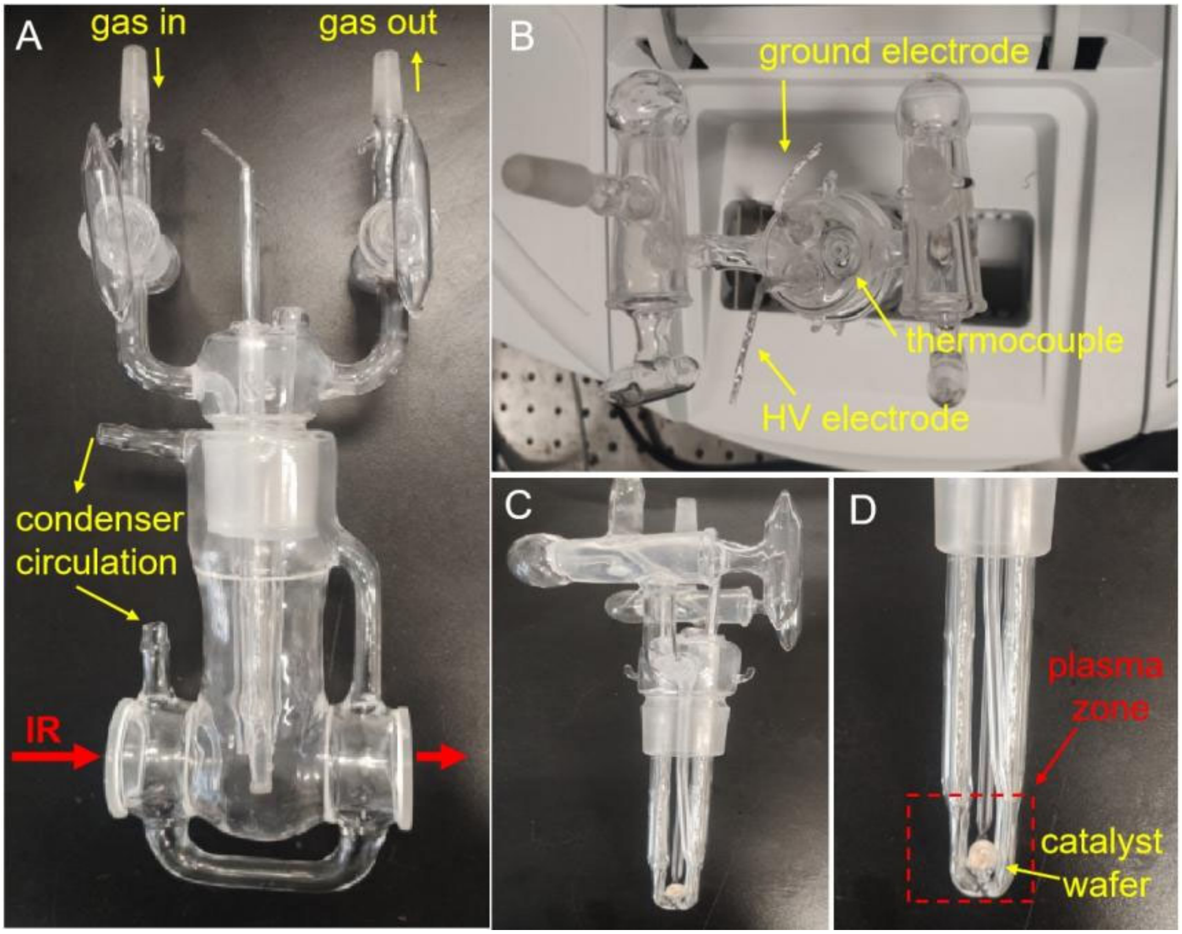

Figure S2. Schematic diagram of the FTIR reaction cell for *in-situ* characterization of plasma catalysis.

The surface functional groups of the catalyst and gas molecules were characterized using a Thermo Nicolet iS10 infrared spectrometer equipped with a rapidly recoverable detector containing heavy hydrogen triethylene glycol salts (DTGS). The instrument's resolution was set at 4.0 cm^{-1}, with a scanning range from 4000 to 400 cm^{-1}, and each scan was repeated 64 times. Catalyst samples weighing 0.05 g were initially ground to fine powder in a mortar and pestle, then pressed into self-supporting discs with a diameter of 8 mm, and subsequently placed into the infrared cell fitted with CaF_2 windows. The plasma power source was activated, and the discharge mode was initiated to collect signals. The FTIR cell was heated by the plasma, and a thermocouple was employed to monitor real-time temperature.

2. Catalyst preparation and characterization

Catalyst preparation: All catalysts were prepared by wet impregnation of an aqueous solution onto CeO_2 (commercial), which belongs to non-porous material with a small BET surface area (16.2 m^2 g^{-1}) and pore volume (0.053 cm^3 g^{-1}). Indeed, this is clear from our nitrogen physisorption experiments (see Table S1 and Figure S3). While the adsorption-desorption isotherm exhibits an H3 hysteresis loop, indicating the presence of slit-like pores within the structure, this can be explained by the extremely small grain size of CeO_2. To achieve a uniform particle size for the packing material before the reaction, we formed CeO_2 granules of consistent size through a physical pressing method. This process promotes the accumulation of CeO_2 grains, leading to the formation of slit-like pores. Nevertheless, CeO_2 is clearly a non-porous material, based on the small amount of N_2 adsorption and the fact that the external surface area, indicated by nitrogen physisorption is greater than the BET surface area. This means that all Cu species are dispersed on the external surface of the support, and thus exposed to the plasma species, without severe presence of gradients in structure, chemical composition and morphology. Metal salts ($Cu(NO_3)_3.3H_2O$, Sigma-Aldrich) were dissolved in distilled water, and then the support was added and stirred for 5 h at room temperature. After that, the solution was dried in air at 60 °C. The resulting solid lumps were crushed into powder, and then dried at 120 °C for 12 h before being calcined in air at 540 °C for 5 h.

Catalyst characterization: X-ray diffraction (XRD) patterns were recorded on a SmartLab 9KW X-ray diffractometer using Cu Kα radiation (λ=0.15406 nm). The X-ray tube was operated at 240 kV and 50 mA. The data was recorded from 5° to 85°. The scanning speed was 10° /min with a step size of 0.02°. The microstructure characterization of the catalysts was examined by high resolution transmission electron microscopy (HRTEM) (Tecnai G2 F30 S-Twin), with an energy-dispersive X-ray spectrometer (EDXS), and by scanning transmission electron microscopy (STEM) with bright field (BF) and dark field (DF), at an accelerating voltage of 300 kV. The powdered catalyst was dispersed in ethanol, and the mixture was sonicated to obtain a monodisperse catalyst solution before dropping the solution on a TEM grid (ultrathin carbon membrane coated, 300 mesh). After drying, the samples were imaged. X-ray photoelectron spectroscopy (XPS) was conducted using a Thermo Fisher ESCALAB XI+ with a monochromatic Al K_α X-ray source (hv = 1486.6 eV) at a power of 150 watts and an analysis spot size of 500 micrometers. The pass energy of the wide-scan energy analyzer was fixed at 100 eV, while that of the narrow-scan energy analyzer was fixed at 20 eV. Characterization of Cu species on the catalyst surface was performed by a UV-Visible (UV-Vis) spectrophotometer (UV-550, Agilent, USA) with integrating sphere attachment (built-in dra2500). Raman analysis was performed with a confocal micro-Raman spectrometer model in Via Qontor with radiation of 532 nm. The redox behavior of the catalysts was investigated by hydrogen temperature programmed reduction (H_2-TPR) using a chemisorption instrument (Quantachrome ChemBET 3000). The TPR analysis was carried out in a H_2/Ar mixture flow (10 % H_2, 120 cm^3 /min) from room temperature to 1073 K with a heating rate of 10 K/min. The H_2 concentration in the tail gas was monitored by the TCD, to indicate the H_2 consumption as a function of temperature. Electron paramagnetic resonance (EPR) analysis was performed by a Bruker (E500) operating at the X d (~9.42 GHz) at 100 K with liquid nitrogen and 100 kHz.

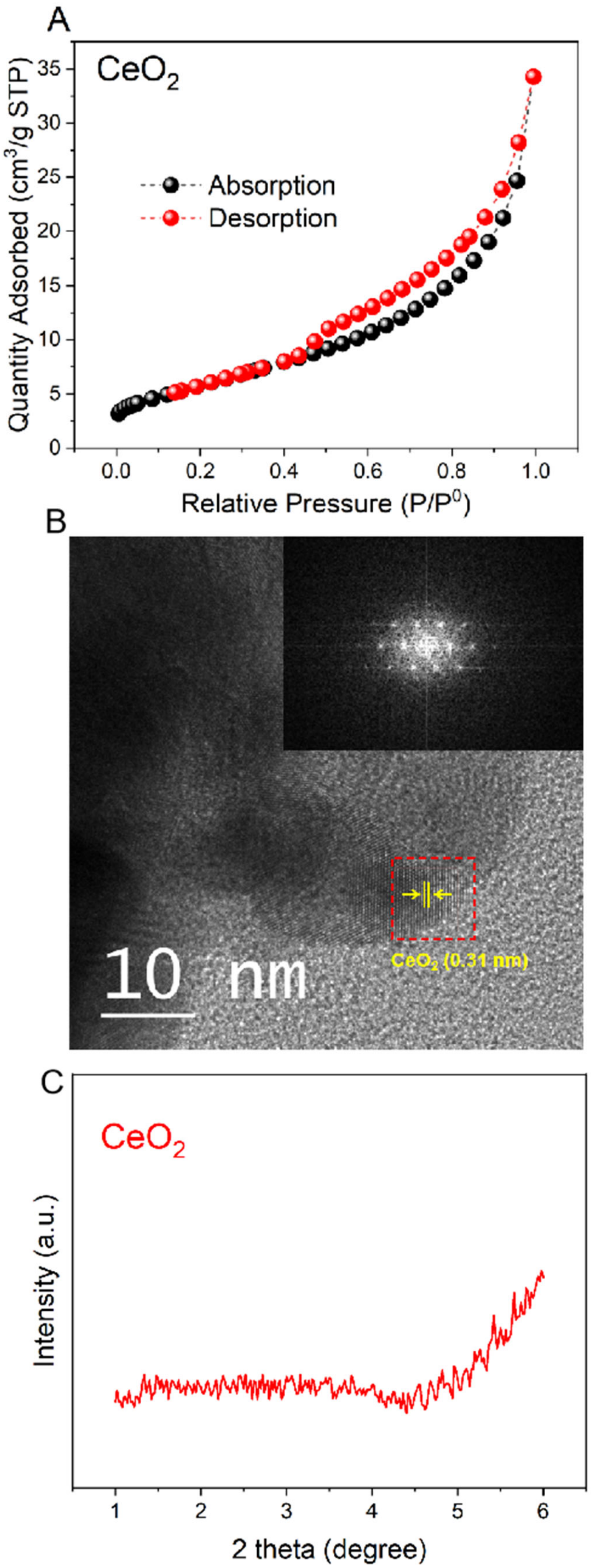

Figure S3. Characterization of CeO_2 (A)the adsorption-desorption isotherms of N_2, (B) HRTEM image, and (C) the small-angle XRD patterns.

In Figure S3A, the adsorption-desorption isotherm exhibits an H_3 hysteresis loop, indicating the presence of slit-like pores within the structure, this can be explained by the extremely small grain size of CeO_2. To achieve a uniform particle size for the packing material before the reaction, we formed CeO_2 granules of consistent size through a physical pressing method. This process promotes the accumulation of CeO_2 grains, leading to the formation of slit-like pores. Nevertheless, CeO_2 is clearly a non-porous material, based on the small amount of N_2 adsorption and the fact that the external surface area, indicated by nitrogen physisorption is greater than the BET surface area. Moreover, in Figure S3B, CeO_2 displays distinct and well-organized crystal diffraction patterns, which reflect the periodic structure and lattice parameters of CeO_2 crystals. This observation further confirms that CeO_2 is not a mesoporous material, since mesoporous materials are amorphous. In the XRD patterns, as shown in Figure S3C, no significant diffraction peaks appeared in the small-angle region, indicating that the CeO_2 support is non-porous (Because porous materials usually exhibit one or more diffraction peaks in the small-angle region, with the positions and intensities of these peaks related to pore size and structure.).

3. Comparison of plasma alone, Plasma + CeO_2, and Plasma + CuO/CeO_2.

3.1 Reaction performance

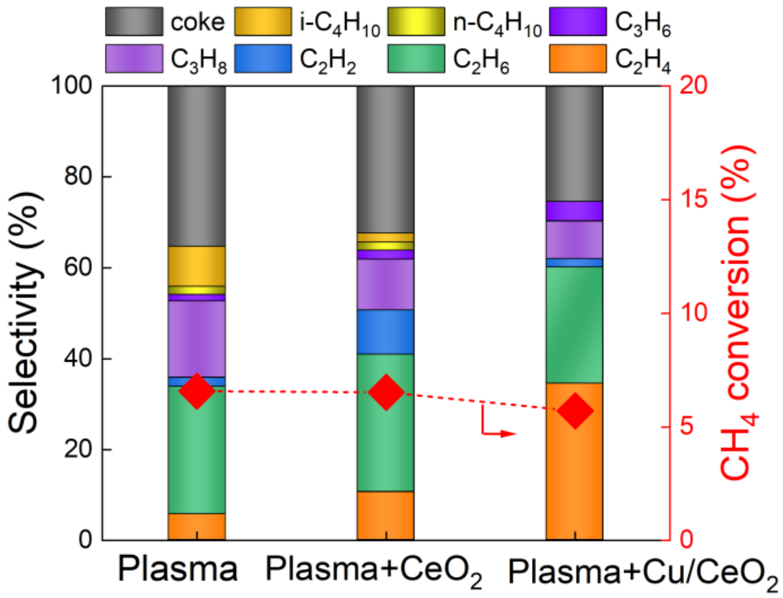

Figure S4. Comparison of C_2H_4 selectivity for the cases of Plasma alone, Plasma + CeO_2, and Plasma + CuO/CeO_2 with similarly CH_4 conversion. (reaction conditions: 10 wt % CuO loading, CH_4/Ar = 1:1, flow rate = 20 ml/min, 14 kHz discharge frequency)

By adjusting plasma input power (10.0 W for plasma only, 15.5 W for plasma+CeO_2, 15.4 W for plasma+CuO/CeO_2), we obtained similar CH_4 conversion for Plasma alone, Plasma+CeO_2, and Plasma+CuO/CeO_2. However, Plasma+CuO/CeO_2 still show the best C_2H_4 selectivity, highlighting that the CuO/CeO_2 catalyst is effective for producing C_2H_4.

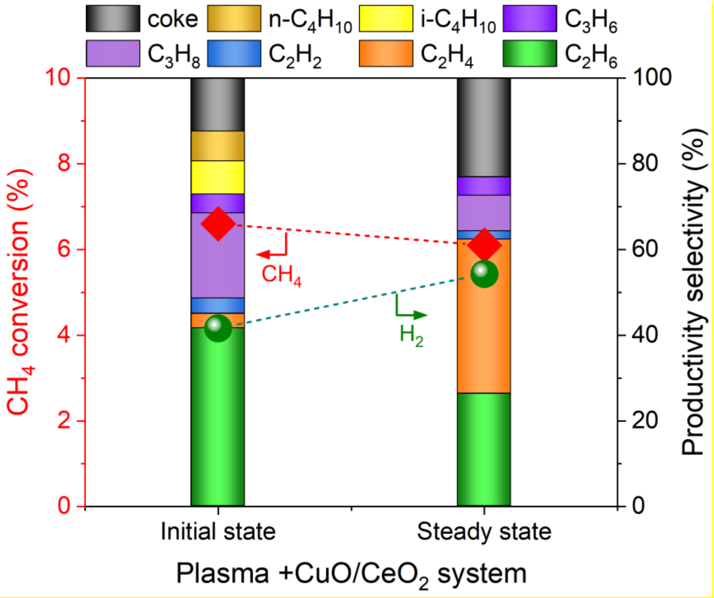

Figure S5. Comparison of performances between initial state and steady state in the case of Plasma + CuO/CeO_2. (reaction conditions: 10 wt % CuO loading, CH_4/Ar = 1:1, flow rate = 20 ml/min, weight of catalyst=1.08 g, WHSV=1.39 h^{-1}, 15.4 W input power, 14 kHz discharge frequency)

In Figure S5, the main products in the initial state are alkanes, with the highest selectivity for C_2H_6 (41.6%). The selectivity of the other hydrocarbon products—C_2H_4, C_2H_2, C_3H_8, C_3H_6, i-C_4H_{10}, n-C_4H_{10} and coke—are 3.4%, 3.6%, 19.9%, 4.4%, 7.7%, 7% and 12.4%, respectively. In the steady state of the “Plasma + CuO/CeO_2” system, the main product is C_2H_4 (36.1%), while the selectivity of the other hydrocarbons—C_2H_6, C_2H_2, C_3H_8, C_3H_6 and coke—are 26.3%, 1.9%, 8.3%, 4.3% and 23.1%, respectively. Correspondingly, the selectivity of H_2 in the initial and steady states are 41.6% and 54.3%, respectively.

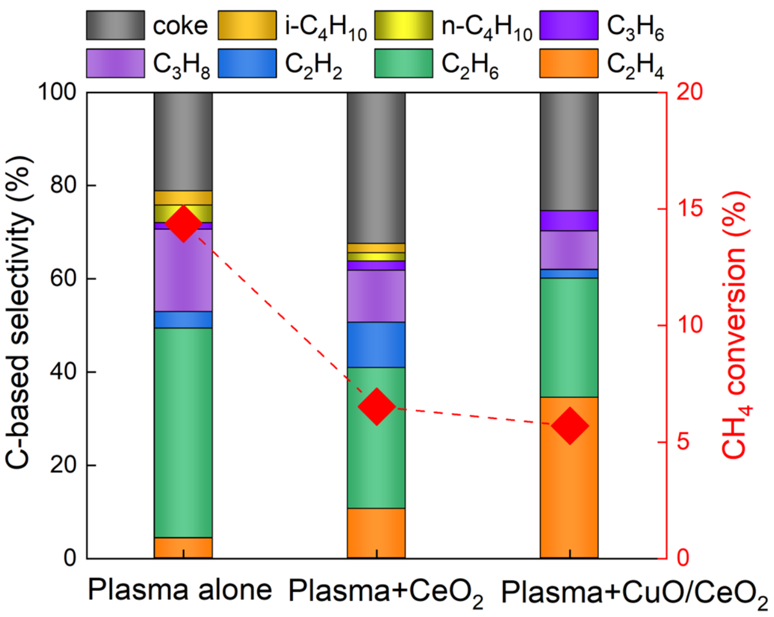

Figure S6. Comparison of CH_4 conversion and C-base product selectivity for the cases of Plasma alone, Plasma + CeO_2, and Plasma + CuO/CeO_2. (reaction conditions: 10 wt % CuO loading, CH_4/Ar = 1:1, flow rate = 20 ml/min, 15-16 W input power, 14 kHz discharge frequency)

With similar plasma input power, the reduction in CH_4 conversion (as shown in Figure S6) was mainly attributed to the high dielectric constant and insulating properties of the CeO_2 support. These properties effectively suppress the electric field intensity and enhance the polarization effect, collectively reducing the discharge intensity, which in turn lowers the CH_4 conversion rate.

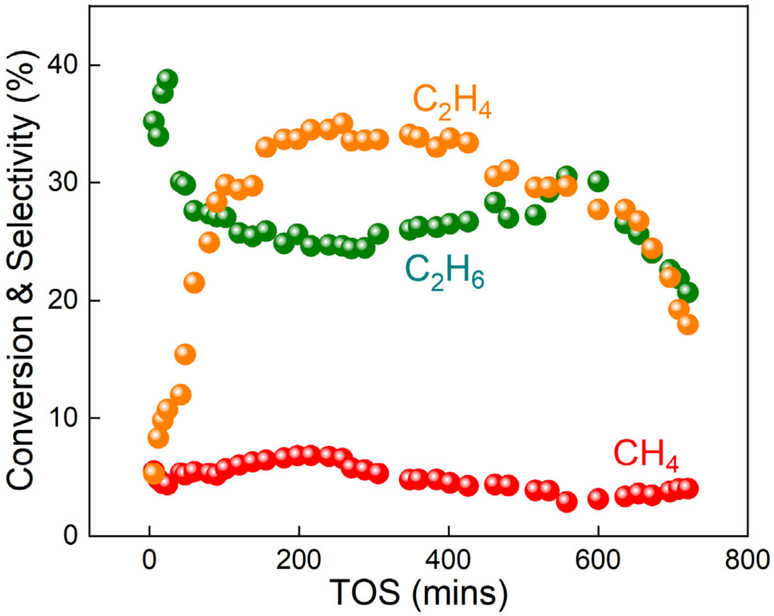

Figure S7. Reaction stability for NOCM under Plasma+CuO/CeO_2 system.

Figure S7 shows the reaction stability of NOCM under the Plasma+CuO/CeO_2 system. During the first 200 min of the reaction, the ethylene selectivity gradually increases while the ethane selectivity decreases. As the reaction continues, the ethylene selectivity starts to decrease and the ethane selectivity begins to increase. The methane conversion also gradually decreases, likely due to the accumulation of carbon deposits, which poisons the active sites of the catalyst.

3.2 Gas chromatogram (GC) results

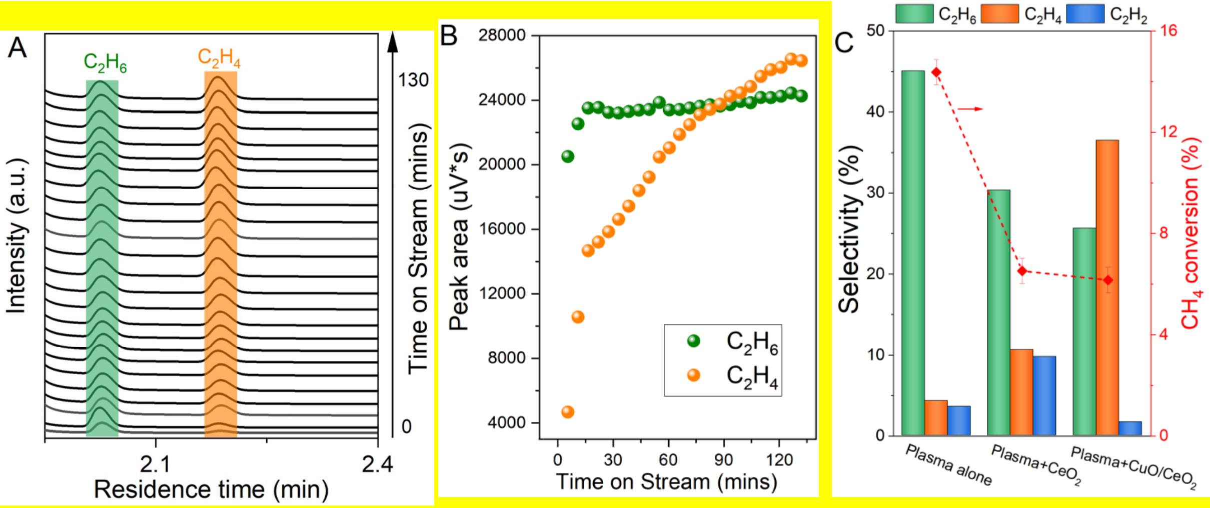

Figure S8. Gas chromatogram (GC) profiles of the exhaust gas from "plasma + CuO/CeO_2" (A) , peak area of C_2H_6 and C_2H_4 from GC profiles as a function of time on stream in (B), and comparison of conversion and selectivity for Plasma alone, Plasma + CeO_2, and Plasma + CuO/CeO_2 (C) (the steady state is reached after 115 mins).

Figure S8A shows the gas chromatogram (GC) profiles of the exhaust gas from "plasma + CuO/CeO_2" with time on stream, and the peaks of C_2H_6 and C_2H_4 have been displayed. It can be seen from Figure S8B that the peak areas of C_2H_4 gradually increases with time on stream, surpasses that of C_2H_6 at ca. 75 min, and finally reaches a stable value at ca. 115 min. The above mentioned GC profiles show strong evidences for the gradually increased C_2H_4 selectivity in the case of "plasma + CuO/CeO_2".

3.3 reaction pathways

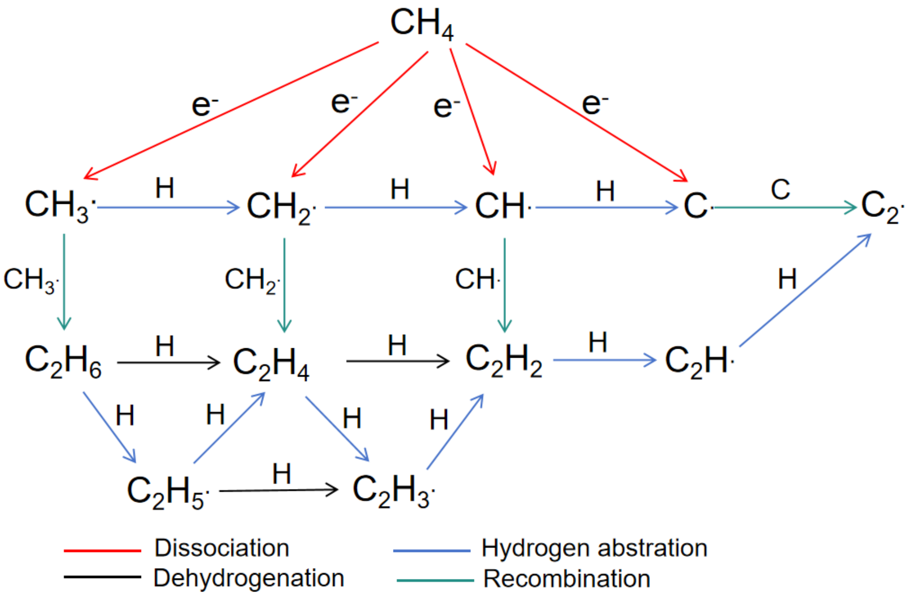

Figure S9. The possible reaction pathways for CH_4 to C_2 in the DBD plasma.

The predominant reaction pathways for the production of C_2 hydrocarbons in DBD plasma activation of CH_4 are shown in Figure S9 Each color represents the type of reaction occurring. Among all generated species, radicals play a key role in determining the reaction pathways and the distribution of products inside the plasma. The activation of CH_4 starts with electron impact dissociation to generate CH_x radicals (CH_x·).[2, 3] Model calculations have pointed out that reaction ($e^- + CH_4 \rightarrow e^- + CH_3 \cdot + H \cdot$) is responsible for 79% of the total electron impact dissociation of CH_4, while reactions ($e^- + CH_4 \rightarrow e^- + CH_2 \cdot + H_2$) and ($e^- + CH_4 \rightarrow e^- + CH \cdot + H_2 + H \cdot$) are responsible for 15% and 5%, respectively.[4] Similar results were reported by Yang.[5]

CH_x· further undergo recombination reactions, producing C_2H_6, C_2H_4, and C_2H_2 hydrocarbons.[6, 7] On the other hand, successive dehydrogenation reactions of C_2H_6 are also possible steps for the production of C_2H_5·, C_2H_4, C_2H_3·, ,C_2H_2, and C_2H·, forming C_2H_3· and C_2H· intermediates,[8] which subsequently contribute to the formation of deposits.

3.4 Discharge parameters

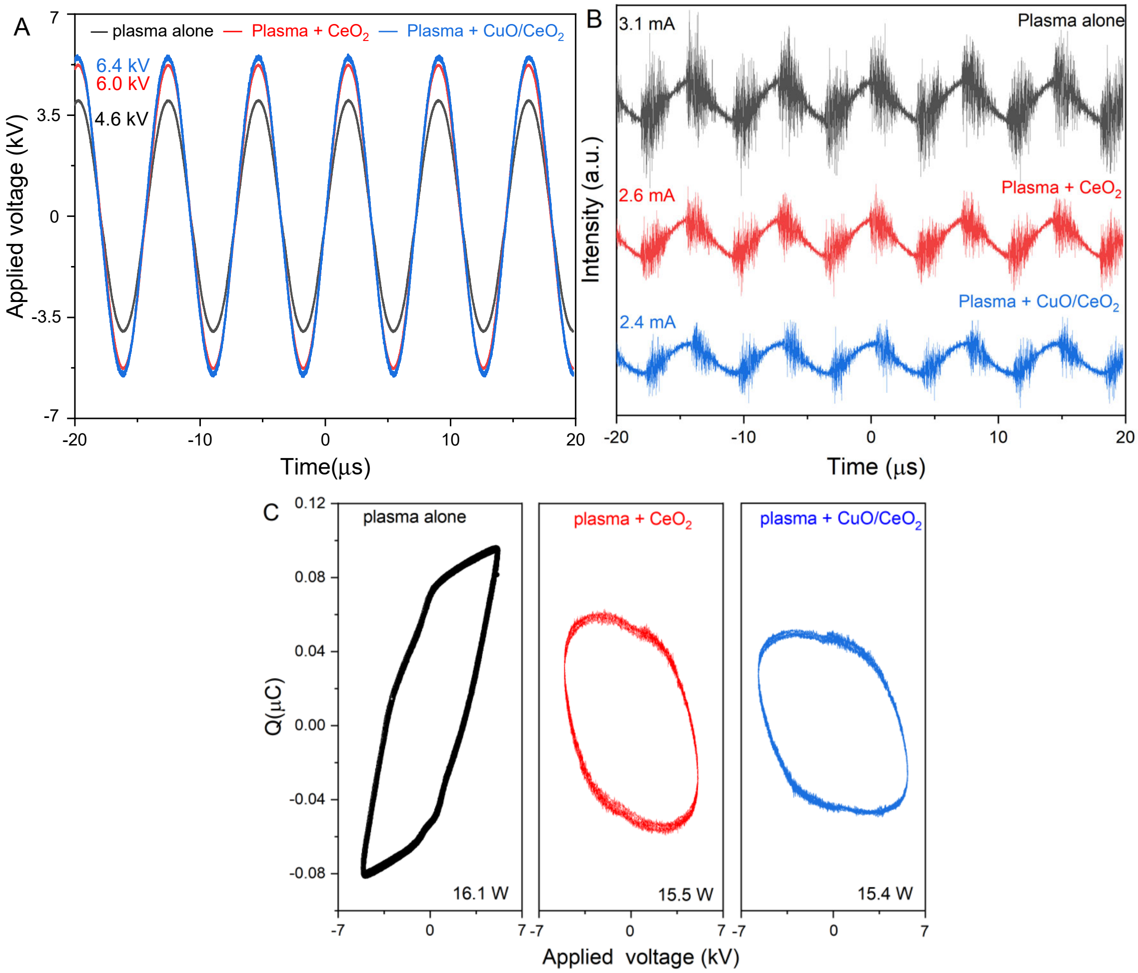

Figure S10. Comparison of discharge parameters for the cases of plasma alone, plasma + CeO_2, and plasma + CuO/CeO_2 catalyst. (A) Discharge voltage, (B) Current intensity, (C) Lissajous plots. (10 wt % CuO loading, CH_4/Ar = 1:1, flow rate = 20 ml/min, 1.08 g packing material, WHSV=1.39 h^{-1}, 15-16 W input power, 14 kHz discharge frequency)

Figure S10 A indicates that the amplitude of the applied voltage increases from 4.6 kV (plasma alone system) to 6.4 kV (plasma + CuO/CeO_2 system), while the discharge current intensity decreases from 3.1 mA to 2.4 mA (Figure S10 B). The discharge power remains fairly constant at 15-16 W, despite the very different shape of the Lissajous plots, as shown in Figure S10 C. Consequently, to maintain equivalent power levels, the "plasma + CeO_2" and the "plasma + CuO/CeO_2" systems require the input of additional external voltage.

3.5 OES spectra

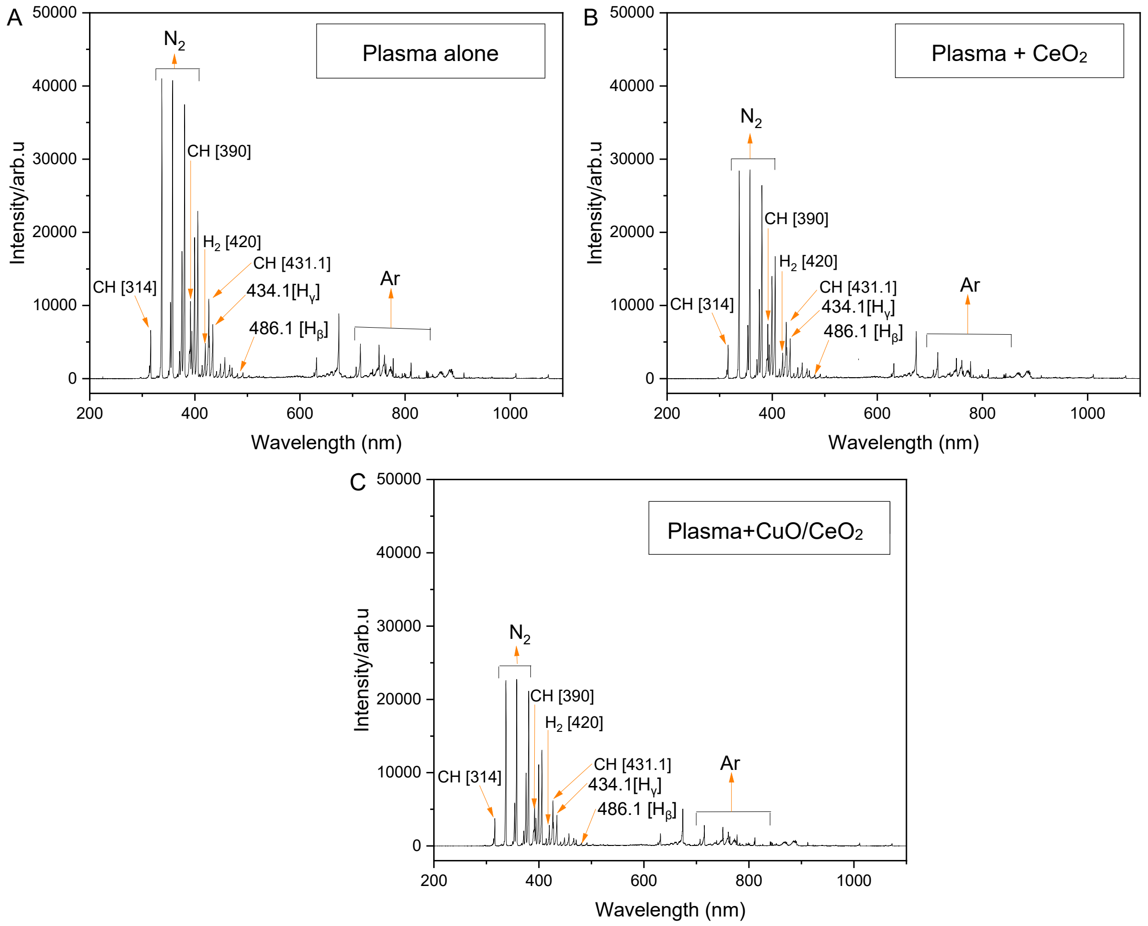

Figure S11. Optical emission spectrum (OES) of a CH_4/Ar discharge in (A) plasma alone, (B) plasma + CeO_2, and (C) Plasma +CuO/CeO_2. (10 wt % CuO loading, CH_4/Ar = 1:1, flow rate = 20 ml/min, 1.08 g packing material, WHSV=1.39 h^{-1}, 15-16 W input power, 14 kHz discharge frequency)

Figure S11 illustrates the OES spectrum of the CH_4/Ar plasma. The OES spectrum intensity of "plasma alone" (Figure S8 A) is higher than for "plasma + CeO_2" (Figure S11 B) and "plasma + CuO/CeO_2" (Figure S11 C). The peaks at 431.1 nm, 390 nm and 314 nm are assigned to the CH· species,[9, 10] which are considered as precursors for amorphous carbon deposition. Besides the hydrocarbon radicals, excited hydrogen-related species, H_2 (420 nm), H_β (486.1 nm) and H_γ (434.1 nm), and argon related species (690-850 nm) are also detected.[10, 11]

4. XRD patterns

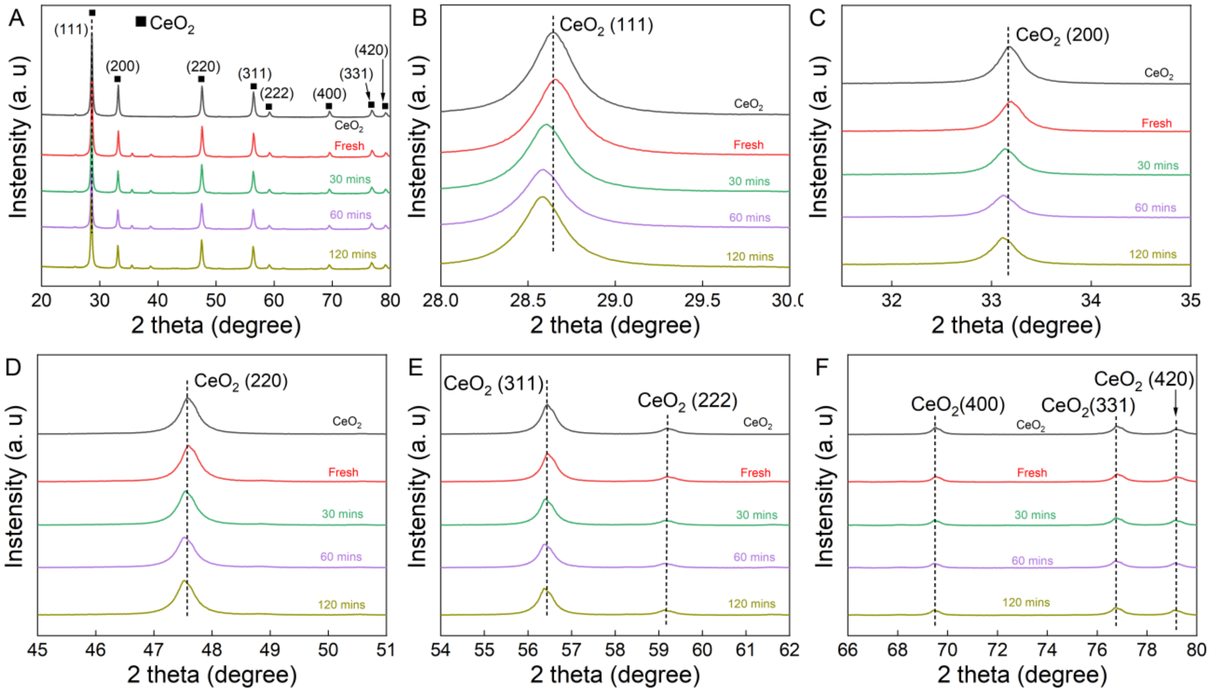

Figure S12. (A) X-ray diffraction (XRD) patterns of the catalysts; enlarged view of the (111) crystal plane (B), (200) crystal plane (C), (220) crystal plane (D), (311) and (222) crystal plane (E), and (400), (331), and (420) crystal plane (F) for CeO_2.

In XRD spectra, usually, compared with the reflection peak of CeO_2, a slight shift is observed for the serial Cu-Ce binary oxides. This suggests that small Cu^{2+} ions dissolve into the CeO_2 lattices, replacing the Ce^{4+} species. Considering that the radius of Cu^{2+} ion (0.073 nm) is smaller than that of Ce^{3+} (0.110 nm) or Ce^{4+} ion (0.097 nm), a Cu-Ce solid solution might be formed.[12-16] Obviously, the diffraction pattern reflections of CeO_2 systematically shifted to higher degree in CuO/CeO_2-Fresh catalyst in Figure S12, suggesting that Cu^{2+} has been substituted into the CeO_2 lattice[17] and altered the unit cell parameter of CeO_2, [18,19] because of the smaller ionic radius of Cu^{2+} (0.073 nm) than that of Ce^{4+} (0.097nm). The drop of lattice parameter calculated by XRD is presented in Table S2. However, the lattice parameters of CeO_2 in CuO/CeO_2-0.5h, CuO/CeO_2-1h, and CuO/CeO_2-2h catalysts in this experiment are larger, which could be explained because the modified metal and copper enter the CeO_2 lattice, accompanied by the formation of more Ce^{3+}, and the ionic radius of Ce^{3+} (0.110 nm) was larger than the ionic radius of Ce^{4+}, which led to the larger cell parameters.[20]

5. UV-vis spectra

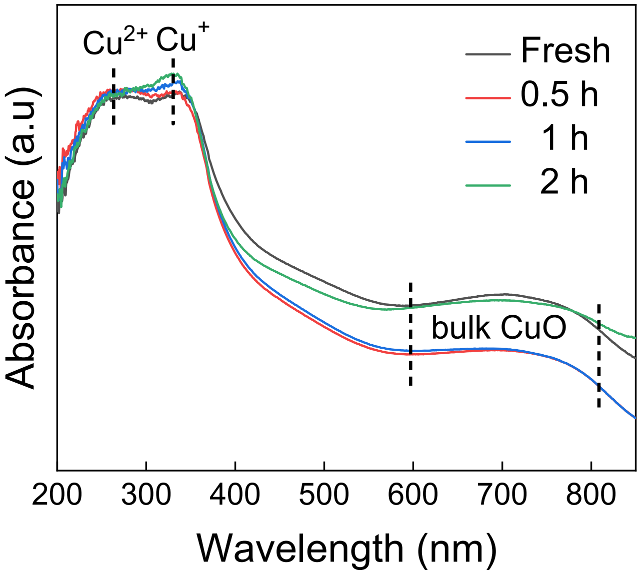

Figure S13. UV-vis spectra of the fresh and spent CuO/CeO_2 catalysts

In the UV-vis diffuse reflectance spectra (Figure S13), the broad band at 600-800 nm corresponds to the d-d transition of bulk CuO, indicating that bulk CuO was gradually reduced from the CuO/CeO_2-Fresh samples during the 2 h reaction time. The absorption band (245-285 nm) corresponds to the ligand-metal charge transfer band of the Cu^{2+} fraction.[11, 21] A sharp absorption band at 330 nm of Cu^{+} increases as the reaction progresses,[21, 22] which can be well explained by the generation of asymmetric oxygen vacancies at the $CuO-CeO_2$ interface during the induction period (formation of Cu^{+} -O_v-Ce^{3+} species).

6. Raman spectra

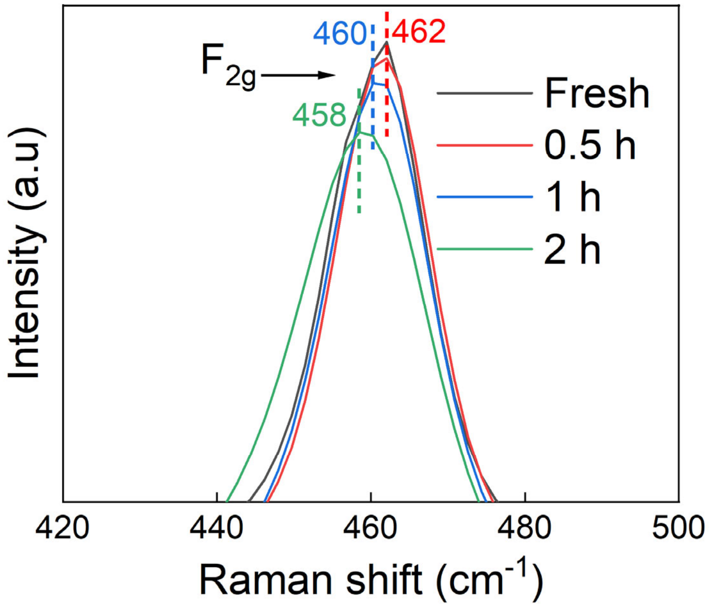

Figure S14. Raman spectra of the fresh and spent CuO/CeO$_2$ catalysts

The F$_{2g}$ band was observed to be slightly shifted from 462 cm^{-1} to 458 cm^{-1} (Figure S14), which can be ascribed to the fact that the doped CuO species and the formation of Cu-O$_x$-Ce species lead to the extension of the Ce−O bond lengths in the interface, resulting in the low-energy shifts in the Raman spectra. [23, 24]

7. XPS spectra

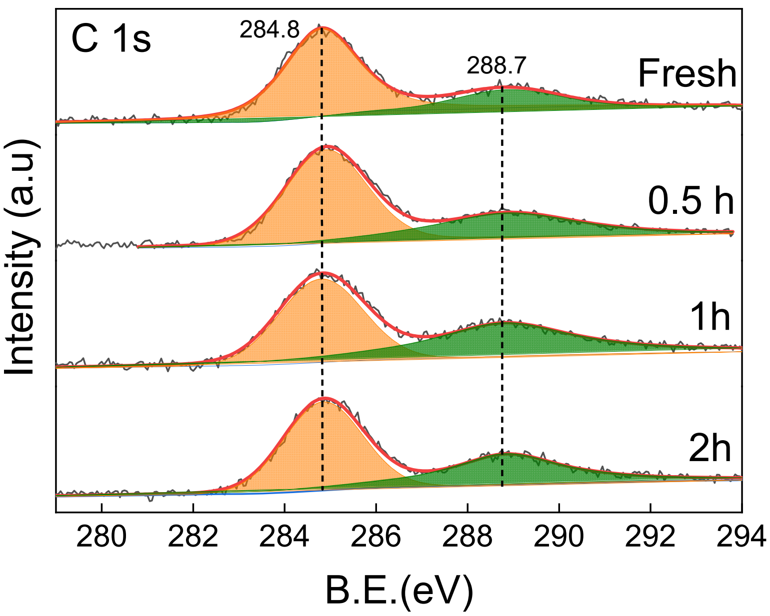

Figure S15. C1s XPS spectra of the CuO/CeO_2 catalysts at different reaction times.

The peaks of 284.8 eV and 288.7 eV are classified as graphitic carbon and oxidized carbon species, respectively. [25]

8. Catalytic performance of CuO/Al_2O_3, CuO/SiO_2 and CuO catalyst.

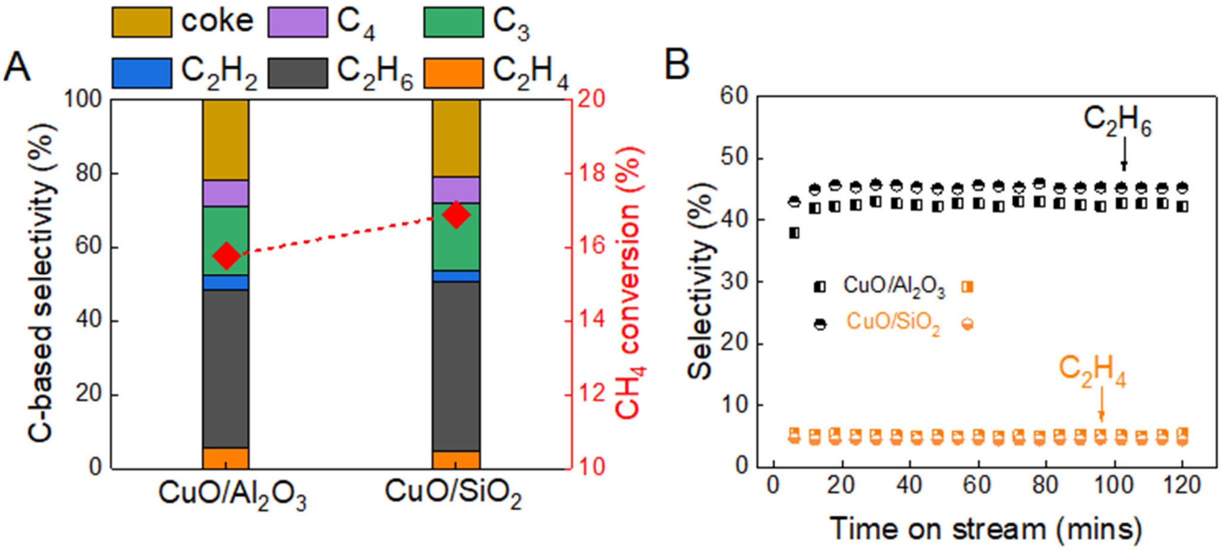

Figure S16. Catalytic performance of CuO/Al_2O_3 and CuO/SiO_2 catalysts in plasma-catalytic NOCM. (A) CH_4 conversion and C-based product distributions, (B) catalytic stability. (10 wt % CuO loading, $CH_4/Ar = 1:1$, flow rate = 20 ml/min, 1.08 g packing material, WHSV=1.39 h^{-1}, 15.4 W input power, 14 kHz discharge frequency)

Figure S16 A shows the CH_4 conversion and C-based product selectivity when CuO/SiO_2 or CuO/Al_2O_3 catalysts were combined with the plasma. C_2H_6 is the main product for both CuO/SiO_2 and CuO/Al_2O_3 catalyst, while the C_2H_4 selectivity is as low as 5 %. Furthermore, as shown in Figure S16 B, no induction period is observed for the CuO/SiO_2 and CuO/Al_2O_3 catalysts, which demonstrates the uniqueness of the CuO/CeO_2 catalysts in plasma-catalytic NOCM reaction.

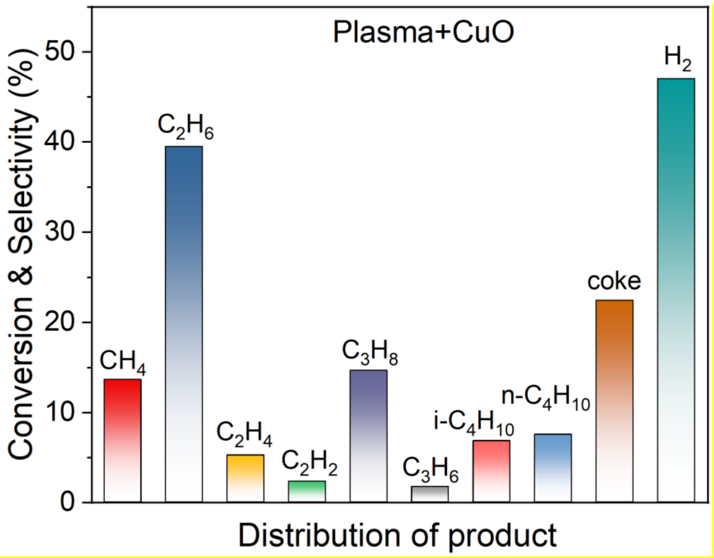

Figure S17. CH_4 conversion and product selectivity for Plasma+CuO system

Figure S17 illustrates the CH_4 conversion and product selectivity in the Plasma+CuO system. The primary products are alkanes. Compared to the plasma system, the CH_4 conversion experiences a slight decrease, while the selectivity for H_2 increases. CuO was synthesized by calcining copper nitrate at 540 °C for 3 hours.

9. *In-situ* FTIR spectra on CuO/CeO_2 catalyst

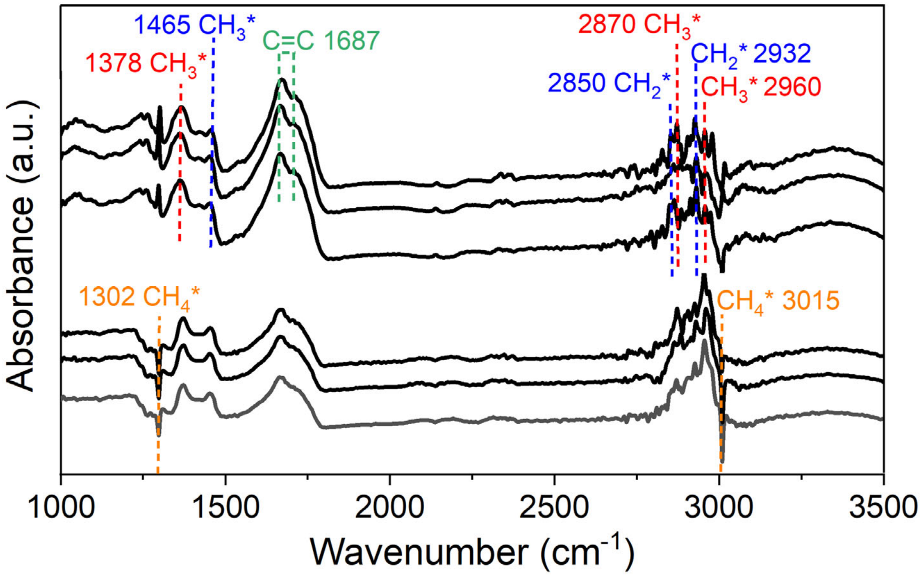

Figure S18. *In-situ* FTIR spectra for NOCM to C_2H_4 in plasma over CuO/CeO_2 catalyst.

The IR spectra were obtained after subtraction of the background spectrum of the sample before adsorption. The peaks related to CH_4 can be easily seen at wavenumbers of 3015 cm^{-1} and 1302 cm^{-1}, as shown in Figure S18. The 1300–1500 cm^{-1} band is associated with the C–H bending vibration, in particular, the peaks at 1378 cm^{-1} and 1465 cm^{-1} are due to the C–H bending of $–CH_3$ groups. The absorption band at 2800–3000 cm^{-1} is assigned to the C–H stretching vibration, and the two peaks at 2960 and 2870 cm^{-1} are due to the C–H stretching of CH_3* groups, while the two peaks at 2932 cm^{-1} and 2850 cm^{-1} are classified to CH_2* groups. The vibrational band at 1687 cm^{-1} is assigned to π–bonded or σ–bonded C=C, which suggests the presence of $CH_2=CH_2$.

10. C_2H_6 conversion and product selectivity in Plasma alone and Plasma+CuO/CeO$_2$ system

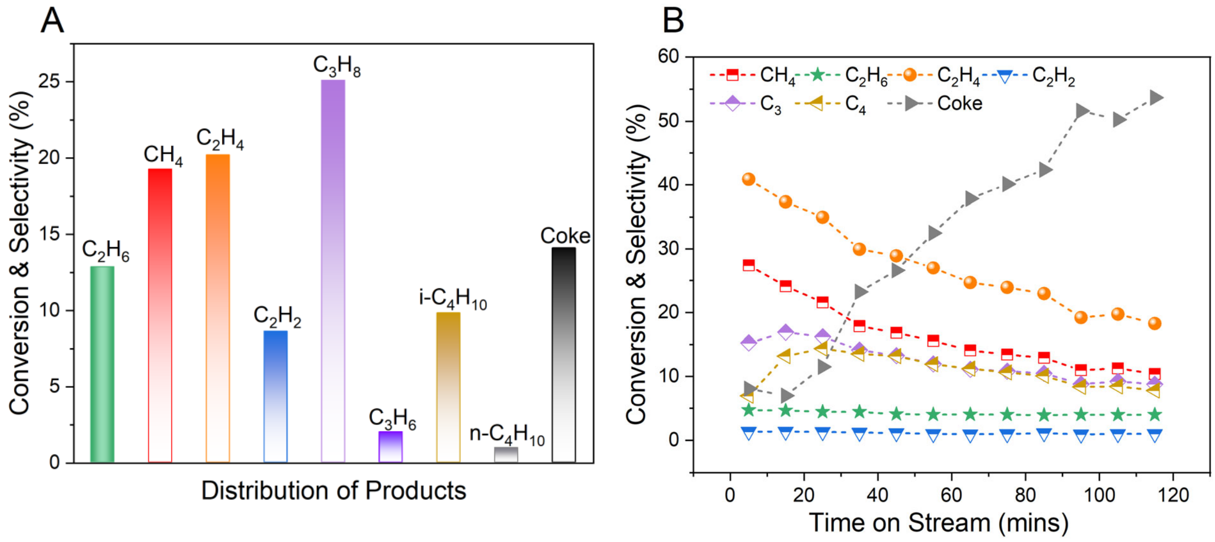

Figure S19. Ethane conversion and product selectivity in (A) Plasma alone system and (B) Plasma+CuO/CeO$_2$ system, (Feed flow rate =20 ml/min)

Figure S19A presents the conversion and product selectivity of non-oxidative conversion of C_2H_6 in a plasma environment. The result indicates that the main product is C_3H_8. In other words, under the relatively mild temperature conditions of this system, C_2H_6 is more likely to produce C_3H_8 rather than C_2H_4. Figure S19B illustrates the conversion of C_2H_6 in the plasma + CuO/CeO$_2$ system. As the reaction progresses, the selectivity for C_2H_4 gradually decreases. However, in the CH_4 conversion by plasma + CuO/CeO$_2$ system (see Figure 1C in the main paper), the selectivity for C_2H_4 increases over time. This comparison clearly demonstrates that C_2H_4 is not (predominantly) produced from dehydrogenation of C_2H_6. Indeed, if C_2H_4 would be produced from the dehydrogenation of C_2H_6, then the selectivity for C_2H_4 should increase over time. The experimental results, however, show a decrease in C_2H_4 selectivity with time on stream. Therefore, in the CH_4 conversion by plasma + CuO/CeO$_2$ system, C_2H_4 is not primarily produced from the stepwise dehydrogenation of C_2H_6. In Figure S19B, the initial oxidation state (CuO) favors C_2H_6 dehydrogenation to produce C_2H_4. As the reaction progresses, CuO is gradually reduced to metallic Cu, leading to a decrease in C_2H_4 selectivity. This suggests that Cu sites are not conducive to C_2H_4 production, which contradicts our experimental results. In addition, the conversion of C_2H_6 is very low, indicating that under the same conditions in CH_4 plasma, the conversion of C_2H_6 is also very low and more prone to forming carbon deposits rather than C_2H_4.

11. *In-situ* FTIR spectra on CeO$_2$, CuO/Al$_2$O$_3$, and CuO/SiO$_2$ catalysts

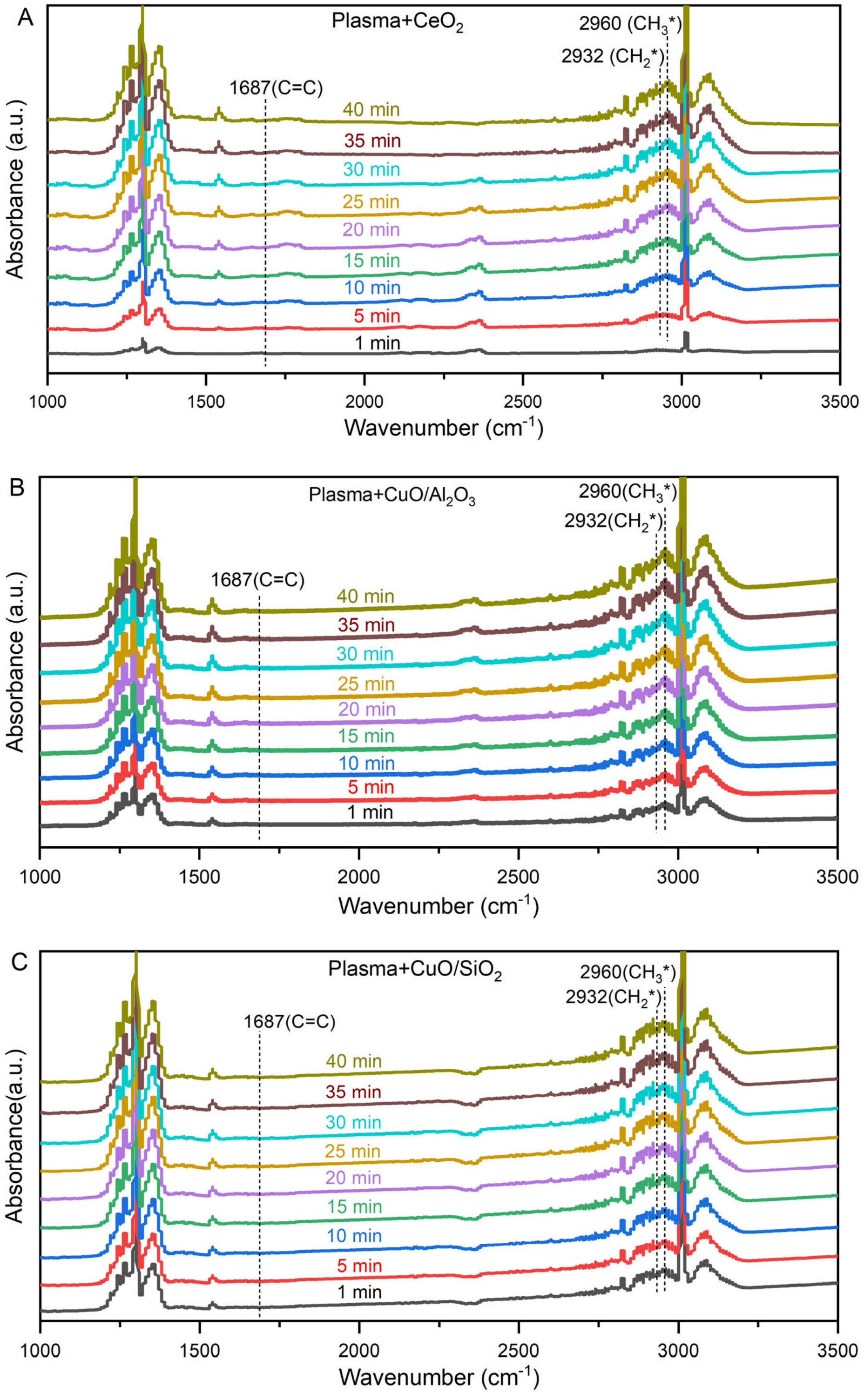

Figure S20. *In-situ* FTIR spectra for NOCM to C$_2$H$_4$ in plasma over (A) CeO$_2$ catalyst, (B) CuO/Al$_2$O$_3$ catalyst, and (C) CuO/SiO$_2$ catalyst.

Figure S20 presents the *in-situ* FTIR results for NOCM by the plasma+CeO$_2$ system, plasma+CuO/Al$_2$O$_3$ system, and plasma+CuO/SiO$_2$ system. It is evident that there are no discernible peaks at 1687 cm^{-1} corresponding to the C=C bond over time on stream. Furthermore, the peak at 2960 cm^{-1} for CH_3* is consistently higher than the peak at 2932 cm^{-1} for CH_2*, which aligns well with the experimental results indicating that the C_2H_6 selectivity is consistently higher than the C_2H_4 selectivity (refer to Figure S6 and Figure S16). If C_2H_6 dehydrogenation to C_2H_4 is a necessary process, then in these systems, all C_2H_6 resulting from CH_3* coupling could undergo dehydrogenation to form C_2H_4. However, the negligible production of C_2H_4 indicates that C_2H_6 dehydrogenation is not the predominant pathway in the plasma-assisted conversion of CH_4.

12. The correlation between CH_2^* intensity and C_2H_4 synthesis rate

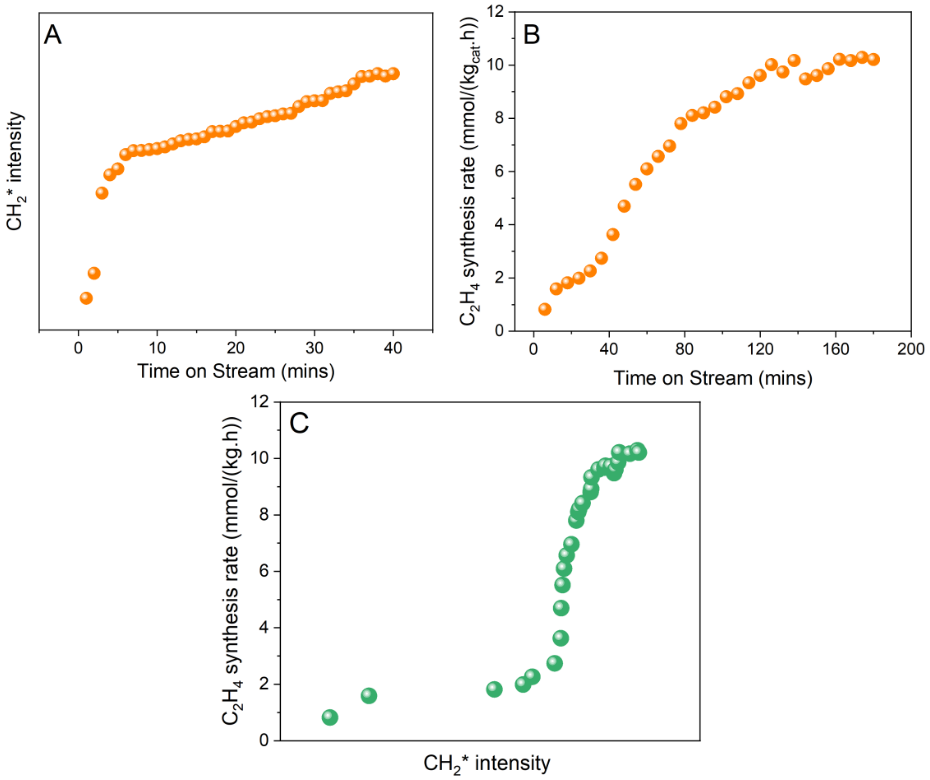

Figure S21. CH_2^* peak intensity in *in-situ* FTIR spectra (A) and C_2H_4 synthesis rate (B) as functions of time on stream. (C) the correlation between CH_2^* intensity and C_2H_4 synthesis rate.

Figure S21 (A,B) shows the CH_2 intensity (obtained from *in-situ* FTIR) and the rate of C_2H_4 production over time. As the reaction progresses, both the intensity of the CH_2^* vibration peaks and the rate of C_2H_4 production increase, showing a positive correlation. Note that during the *in-situ* FTIR characterization, a catalyst wafer (0.05 g, 8 mm in diameter) is used. Compared to the packed bed with 1.08 g of catalyst, it is easier for the plasma species to reach the catalyst surface in a shorter time because the interactions between the plasma species and the catalyst are enhanced. In Figure S21 C, we can observe that at low intensities of CH_2^*, the rate of C_2H_4 production is also low. As the intensity of CH_2^* increases, the rate of C_2H_4 formation correspondingly rises as well. We hypothesize that this trend stems from the initial absence of Cu-O-Ce interface sites, which are crucial for the adsorption and subsequent dehydrogenation of CH_3^* to CH_2^*. As the reaction progresses, the concentration of Cu-O-Ce interface sites increases, enhancing the catalyst's capacity to adsorb CH_3^*. This results in a higher conversion of adsorbed CH_3^* to CH_2^* on the catalyst surface, thereby increasing the production of C_2H_4 through CH_2^* coupling. Consequently, the selectivity towards C_2H_4 gradually improves as the reaction proceeds.

13. Comparison of Cu/CeO_2 and CuO/CeO_2 catalyst

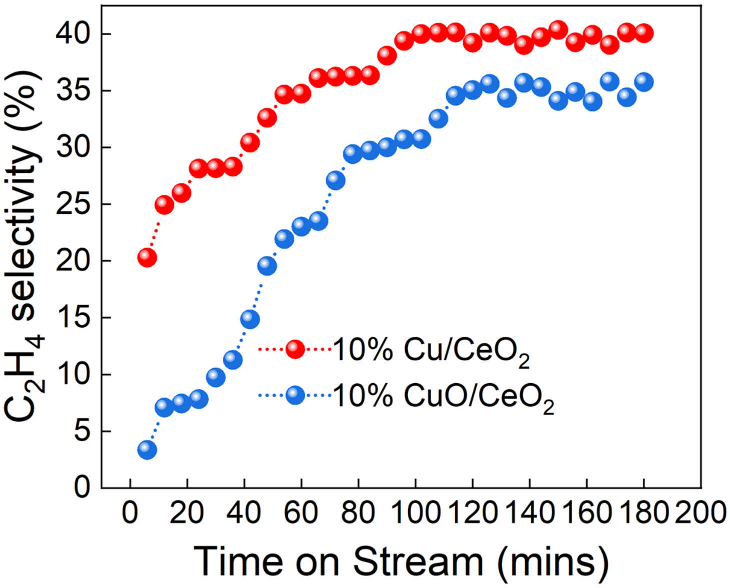

Figure S22. Comparison of the C_2H_4 selectivity in plasma-catalytic NOCM for the Cu/CeO_2 (pre-reduced) and CuO/CeO_2 (without pre-reduction) catalysts with time on stream.

14. Comparison of the Fresh and Spent Cu/CeO$_2$ catalyst.

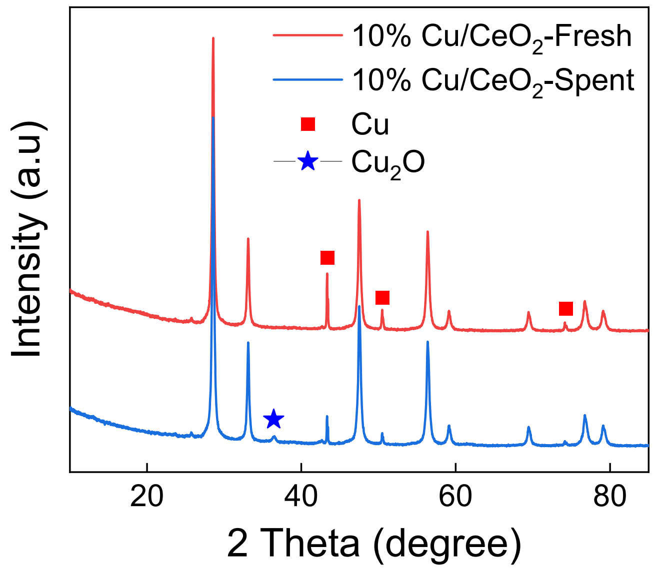

Figure S23. XRD patterns of the fresh and spent Cu/CeO$_2$ catalysts.

15. Comparison of the Fresh CuO/CeO, Cu/CeO and Spent Cu/CeO catalyst.

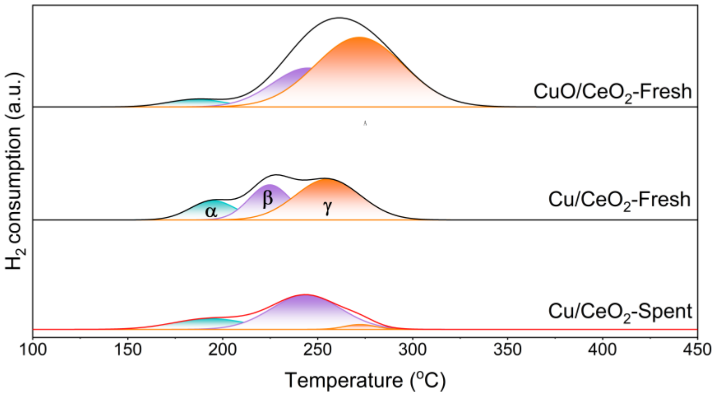

Figure S24. H_2-TPR spectra for fresh 10% CuO/CeO_2, fresh 10% Cu/CeO_2, and spent 10% Cu/CeO_2

Table S1 Texture properties of the CeO_2 support and Cu-based catalysts

Catalysts	BET surface area (m^2 g^{-1})	Average pore diameter (nm)	Pore volume (cm^3 g^{-1})	t-Plot External Surface Area (m^2 g^{-1})
CeO_2	16.2	8.8	0.053	24.6

Table S2. Main electron impact CH_4 dissociation reactions in DBD plasma, along with their threshold energy and the rate coefficient (calculated by integrating the energy-dependent cross section over the electron energy distribution function, *f*(e)).

Reaction	ε_{th},[a] eV	*K*,[b] cm^3/s
$e^- + CH_4 \rightarrow e^- + CH_3\cdot + H\cdot$	8.8	$f(\varepsilon), 5 \times 10^{-10}$
$e^- + CH_4 \rightarrow e^- + CH_2\cdot + H_2$	9.4	$f(\varepsilon), 1.3 \times 10^{-11}$
$e^- + CH_4 \rightarrow e^- + CH\cdot + H_2 + H\cdot$	12.5	$f(\varepsilon), 1.0 \times 10^{-12}$

[a] ε_{th} is the threshold energy and [b]k is the rate constant.

Table S3 The Unit cell parameters of each catalyst calculated using Bragg equation.

Catalysts	Cell parameter for (111) crystal plane (Å)
CeO_2	5.3930
CuO/CeO_2-Fresh	5.3908
CuO/CeO_2-0.5h	5.4004
CuO/CeO_2-1h	5.4040
CuO/CeO_2-2h	5.4046

Table S4. Chemical composition and properties of catalysts, as obtained from XPS, H_2-TPR, and Raman spectra.

	XPS			H_2-TPR			Raman
Catalyst	$Cu^+/(Cu^++Cu^{2+}+Cu^0)$ (%)	$Ce^{3+}/(Ce^{3+}+Ce^{4+})$ (%)	$O_v/(O_v+O_{latt})$ (%)	$\alpha/(\alpha+\beta+\gamma)$ (%)	$\beta/(\alpha+\beta+\gamma)$ (%)	$\gamma/(\alpha+\beta+\gamma)$ (%)	I_D/I_{F2g} (%)
CuO/CeO_2-Fresh	-	4.8	19.7	13.3	31.0	55.7	287.6
CuO/CeO_2-0.5h	5.2	10.3	30.1	16.2	35.2	48.6	331.6
CuO/CeO_2-1h	7.5	14.8	44.2	14.8	40.7	44.5	352.5
CuO/CeO_2-2h	13.2	18.8	59.7	15.0	60.5	24.5	518.6
Cu/CeO_2	-	-	-	21.8	36.8	41.4	-

Table S-5. the goodness-of-fit of the Cu 2p and the FWHM for the peak fitting

	Goodness-of-fit (X^2)	FWHM for Cu 2p (peak position, eV)					
		934.1	941.1	944.0	952.9	954.6	963.3
Fresh	3.01	3.4	3.5	3.4	-	3.6	3.5
0.5 h	2.16	4.3	3.1	3.4	3.3	4.7	3.0
1 h	4.2	3.8	3.9	3.5	3.2	2.7	3.6
2 h	4.5	3.43	3.5	3.4	3.3	3.6	3.5

Table S-6. the goodness-of-fit of the Ce 3d and the FWHM for the peak fitting

	Goodness-of-fit (X^2)	FWHM for Ce 3d (Peak position, eV)									
		881.6	884.1	887.7	890.2	898.0	900.0	902.1	903.1	908.0	917.6
Fresh	7.5	1.3	3.4	2.3	3.8	1.8	2.5	3.1	2.0	5.3	3.5
0.5 h	6.6	1.9	3.4	2.3	3.9	2.2	2.3	3.5	1.9	5.8	3.4
1 h	7.4	1.8	3.3	3.2	4.0	2.2	2.4	3.3	2.5	6.3	3.6
2 h	7.2	2	3.5	2.2	4.0	2.1	2.7	2.9	2.2	6.2	3.5

Table S-7. the goodness-of-fit of the O 1s and the FWHM for the peak fitting

Goodness-of-fit (X^2)	FWHM for O 1s (Peak position, eV)	
	529.2	531.3
2.4	1.6	3.1
2.2	1.6	2.6
2.7	1.6	2.9
2.1	1.4	3.0

16. References

(1) Wanten, B.; Vertongen, R.; De Meyer, R.; Bogaerts, A. Plasma-based CO2 conversion: How to correctly analyze the performance? *Journal of Energy Chemistry* **2023**, *86*, 180-196. DOI: 10.1016/j.jechem.2023.07.005.

(2) Jo, S.; Hoon Lee, D.; Song, Y.-H. Product analysis of methane activation using noble gases in a non-thermal plasma. *Chemical Engineering Science* **2015**, *130*, 101-108. DOI: 10.1016/j.ces.2015.03.019.

(3) Liu, S. Y.; Mei, D. H.; Shen, Z.; Tu, X. Nonoxidative Conversion of Methane in a Dielectric Barrier Discharge Reactor: Prediction of Reaction Performance Based on Neural Network Model. *The Journal of Physical Chemistry C* **2014**, *118* (20), 10686-10693. DOI: 10.1021/jp502557s.

(4) De Bie, C.; Verheyde, B.; Martens, T.; van Dijk, J.; Paulussen, S.; Bogaerts, A. Fluid Modeling of the Conversion of Methane into Higher Hydrocarbons in an Atmospheric Pressure Dielectric Barrier Discharge. *Plasma Processes and Polymers* **2011**, *8* (11), 1033-1058. DOI: 10.1002/ppap.201100027.

(5) Yang, Y. Direct Non-oxidative Methane Conversion by Non-thermal Plasma: Modeling Study. *Plasma Chemistry and Plasma Processing* **2003**, *23*, 327-346.

(6) Kundu, S. K.; Kennedy, E. M.; Gaikwad, V. V.; Molloy, T. S.; Dlugogorski, B. Z. Experimental investigation of alumina and quartz as dielectrics for a cylindrical double dielectric barrier discharge reactor in argon diluted methane plasma. *Chemical Engineering Journal* **2012**, *180*, 178-189. DOI: 10.1016/j.cej.2011.11.039.

(7) Lü, J.; Li, Z. Conversion of natural gas to C2 hydrocarbons via cold plasma technology. *Journal of Natural Gas Chemistry* **2010**, *19* (4), 375-379. DOI: 10.1016/s1003-9953(09)60082-7.

(8) Indarto, A.; Coowanitwong, N.; Choi, J.-W.; Lee, H.; Song, H. K. Kinetic modeling of plasma methane conversion in a dielectric barrier discharge. *Fuel Processing Technology* **2008**, *89* (2), 214-219. DOI: 10.1016/j.fuproc.2007.09.006.

(9) Chen, G. C.; Li, B.; Lan, H.; Dai, F. W.; Zhou, Z. Y.; Askari, J.; Song, J. H.; Hei, L. F.; Li, C. M.; Tang, W. Z.; et al. Gas phase study and oriented self-standing diamond film fabrication in high power DC arc plasma jet CVD. *Diamond and Related Materials* **2007**, *16* (3), 477-480. DOI: 10.1016/j.diamond.2006.09.023.

(10) I. B. Denysenko, S. X., J. D. Long, P. P. Rutkevych, N. A. Azarenkov, K. Ostrikov. Inductively coupled Ar/CH_4 /H_2 plasmas for low-temperature deposition of ordered carbon nanostructures. *Journal of Applied Physics* **2004**, *95*, 2713. DOI: 10.1063/1.1642762 兴.

(11) Shi, Y. C.; Zhang, Q. J.; Li, J. J.; Chen, G. C. Optical Emission Spectroscopy Measurement of Ar\H₂\CH₄ RF Plasma for Nano-Crystal Diamond Film Deposition. *Advanced Materials Research* **2014**, *1035*, 373-378. DOI: 10.4028/www.scientific.net/AMR.1035.373.

(12) Wang, Z.; Qu, Z.; Quan, X.; Li, Z.; Wang, H.; Fan, R. Selective catalytic oxidation of ammonia to nitrogen over CuO-CeO2 mixed oxides prepared by surfactant-templated method. *Applied Catalysis B: Environmental* **2013**, *134-135*, 153-166. DOI: 10.1016/j.apcatb.2013.01.029.

(13) Xing, Y.; Wu, J.; Liu, D.; Zhang, C.; Han, J.; Wang, H.; Li, Y.; Hou, X.; Zhang, L.; Gao, Z. Different metal (Mn, Fe, Co, Ni, and Zr) decorated Cu/CeO(2) catalysts for efficient CO oxidation in a rich CO(2)/H(2) atmosphere. *Phys Chem Chem Phys* **2024**, *26* (15), 11618-11630. DOI: 10.1039/d3cp06125f From NLM PubMed-not-MEDLINE.

(14) Lu, J.; Wang, J.; Zou, Q.; Zhao, Y.; Fang, J.; He, S.; He, D.; Luo, Y. Catalytic performance of transition metals (Co, Ni, Zn, Mo) doped CuO-Ce0.8Zr0.2O2 based catalysts for CO preferential oxidation in H2-rich streams. *Journal of Alloys and Compounds* **2019**, *784*, 1248-1260. DOI: 10.1016/j.jallcom.2019.01.107.

(15) Qu, Z.; Gao, K.; Fu, Q.; Qin, Y. Low-temperature catalytic oxidation of toluene over nanocrystal-like Mn–Co oxides prepared by two-step hydrothermal method. *Catalysis Communications* **2014**, *52*, 31-35. DOI: 10.1016/j.catcom.2014.03.035.

(16) Shan, W. Reduction property and catalytic activity of Ce1−XNiXO2 mixed oxide catalysts for CH4 oxidation. *Applied Catalysis A: General* **2003**, *246* (1), 1-9. DOI: 10.1016/s0926-860x(02)00659-2.

(17) Li, L.; Zhang, C.; Chen, F.; Xiang, Y.; Yan, J.; Chu, W. Facile fabrication of hollow structured Cu-Ce binary oxides and their catalytic properties for toluene combustion. *Catalysis Today* **2021**, *376*, 239-246. DOI: 10.1016/j.cattod.2020.05.038.

(18) Atribak, I.; Azambre, B.; Bueno López, A.; García-García, A. Effect of NO adsorption/desorption over ceria-zirconia catalysts on the catalytic combustion of model soot. *Applied Catalysis B: Environmental* **2009**, *92* (1-2), 126-137. DOI: 10.1016/j.apcatb.2009.07.015.

(19) Wang, L.; Peng, H.; Shi, S.-l.; Hu, Z.; Zhang, B.-z.; Ding, S.-m.; Wang, S.-h.; Chen, C. Metal-organic framework derived hollow CuO/CeO2 nano-sphere: To expose more highly dispersed Cu-O-Ce interface for enhancing preferential CO oxidation. *Appl Surf Sci* **2022**, *573*. DOI: 10.1016/j.apsusc.2021.151611.

(20) Xiong, Y.; Li, L.; Zhang, L.; Cao, Y.; Yu, S.; Tang, C.; Dong, L. Migration of copper species in Ce(x)Cu(1-x)O(2) catalyst driven by thermal treatment and the effect on CO oxidation. *Phys Chem Chem Phys* **2017**, *19* (32), 21840-21847. DOI: 10.1039/c7cp03735j From NLM PubMed-not-MEDLINE.

(21) Lan, T.; Deng, J.; Zhang, X.; Wang, F.; Liu, X.; Cheng, D.; Zhang, D. Unraveling the Promotion Effects of Dynamically Constructed CuOx-OH Interfacial Sites in the Selective Catalytic Oxidation of Ammonia. *ACS Catalysis* **2022**, *12* (7), 3955-3964. DOI: 10.1021/acscatal.1c05676.

(22) X. Qiu, M. M., K. Sunada, M. Minoshima, M. Liu, Y. Lu, D. Li, Y. Shimodaira, Y. Hosogi, Y. Kuroda, and K. Hashimoto. Hybrid Cu_xO/TiO_2 nanocomposites as risk reduction materials in indoor environments. *ACS Nano* **2012**, *6*, 1609-1618.

(23) Wang, W.-W.; Du, P.-P.; Zou, S.-H.; He, H.-Y.; Wang, R.-X.; Jin, Z.; Shi, S.; Huang, Y.-Y.; Si, R.; Song, Q.-S.; et al. Highly Dispersed Copper Oxide Clusters as Active Species in Copper-Ceria Catalyst for Preferential Oxidation of Carbon Monoxide. *ACS Catalysis* **2015**, *5* (4), 2088-2099. DOI: 10.1021/cs5014909.

(24) Sun, H.; Wang, H.; Qu, Z. Construction of CuO/CeO2 Catalysts via the Ceria Shape Effect for Selective Catalytic Oxidation of Ammonia. *ACS Catalysis* **2023**, *13* (2), 1077-1088. DOI: 10.1021/acscatal.2c05168.

(25) Rodríguez, D. G.; Gleeson, M. A.; Lauritsen, J. V.; Li, Z.; Yu, X.; Hans Niemantsverdriet, J. W.; Kees-Jan Weststrate, C. J. Iron carbide formation on thin iron films grown on Cu(1 0 0): FCC iron stabilized by a stable surface carbide. *Appl Surf Sci* **2022**, *585*. DOI: 10.1016/j.apsusc.2022.152684.